To the Graduate Council:

I am submitting herewith a thesis written by Deana Suzanne Sneyd entitled "Deformation of Ordinary Chondritic Meteorites." I have examined the final copy of this thesis for form and content and recommend that it be accepted in partial fulfillment of the requirements for the degree of Master of Science, with a major in Geology.

Harry Y. McSween

Harry Y. McSween, Major Professor

We have read this thesis
and recommend its acceptance:

Theodore C Labotka

Nicholas B Woodward

Accepted for the Council:

C W Minkel

Vice Provost
and Dean of The Graduate School

STATEMENT OF PERMISSION TO USE

In presenting this thesis in partial fulfillment of the requirements for a Master's of Science degree in Geology at The University of Tennessee, Knoxville, I agree that the Library shall make it available to borrowers under rules of the Library. Breif quotations from this thesis are allowable without special permission, provided that accurate acknowledgment of the source is made.

Permission for extensive quotation from or reproduction of this thesis may be granted by my major professor, or in his absence, by the Head of Interlibrary Services when, in the opinion of either, the proposed use of the material is for scholarly purposes. Any copying or use of the material in this thesis for financial gain shall not be allowed without my written permission.

Signature Deana Sneyd

Date 12/9/86

DEFORMATION OF ORDINARY CHONDRITIC METEORITES

A Thesis

Presented for the

Master of Science

Degree

The University of Tennessee, Knoxville

Deana S. Sneyd

March 1987

DEDICATION

To Jim and Charlotte Sneyd,

with love and gratitude

ACKNOWLEDGMENTS

I would like to thank Hap McSween for his undying enthusiasm and support throughout this project. I am also very appreciative of Nick Woodwards critique of my text. Many of his suggestions and comments proved valuable in making this thesis a more complete document. Niogi Sugiura made all magnetic susceptibility measurements and Ted Lobatka helped to edit the final version of the text. Gordon Nord and the U.S.G.S. very generously allowed me use of their transmission electron microscope and Gordon also supervised and helped me to interpret much of the TEM data. Many students in the department deserve recognition as well, but two in particular stand out. Without the diligence and persistance of Jonny Lewis, the bugs in the computerized strain analysis may never have been worked out. I am especially grateful to Randy Kath, who not only taught me how to make thin sections and the slides for this presentation, but acted as a sounding board for hours on end as I slowly made sense of my data.

ABSTRACT

Chondrule strain and magnetic anisotropy are independent measurements of deformation. For the first time, three-dimensional analyses of strain in chondrules and magnetic susceptibility measurements have been performed on the same ordinary chondritic meteorites. These data reveal direct correlations in shape and orientation of the two strain indicators.

Employing computerized strain analysis techniques, a continuous gradation of strain in chondrules was discovered in fifteen ordinary chondrites. Values of strain range from a maximum in Mezo-Madaras of 17% flattening, with mean ellipsoid axial ratios of 1.15:1.00:0.80, to a minimum strain in Kelly of 3% flattening and axial magnitudes of 1.02:1.00:0.96. The mean ellipsoids generated from the samples predominantly have flattening-type or "pancake" spheroidal shapes and are aligned to produce foliations.

Magnetic susceptibility anisotropy was measured for eight of the samples in which the strain was analyzed and magnitudes of the principal axes of the susceptibility ellipsoids were determined. The susceptibility ellipsoids generated for each sample also have pancake spheroidal shapes. Gradation in degree of magnetic anisotropy development was discovered to be directly proportional to gradation of chondrule strain in the samples. In addition to correspondence in ellipsoid shape, orientation of the c (shortened) axis of the strain ellipsoid aligned subparallel to the X1 (shortened) axis of the magnetic susceptibility ellipsoid in six of the eight samples measured.

A range in the degree of shortening in ordinary chondrites is

indicated by these new strain and magnetic measurements. The shapes the of strain and susceptibility ellipsoids are consistent with the hypothesis that deformation was caused by shortening along the principal minimum axes.

Chondrule deformation was discovered to be due to shock processes using several methods. First, each sample was assigned to a shock facies, based on optical criteria, and plotted against its respective percent shortening. These two variables were shown to correlate. Second, noble gas concentrations were noted to have been depleted with increasing strain. Because depletion of noble gas concentrations is also a function of shock, it is assumed that the strain measured was shock-induced. Transmission electron microscopy analyses of a high-strain and a low-strain sample allowed observation of substructures in olivine grains. The density and distribution of dislocations discovered in both samples provided further evidence for shock deformation. Based on these three shock indicators, it is believed that the chondrule strains and magnetic anisotropies quantified and correlated in this study were formed by dynamic compaction during impacts on chondrite parent bodies.

TABLE OF CONTENTS

SECTION PAGE

LIST OF FIGURES

FIGURE PAGE

LIST OF TABLES

I. INTRODUCTION

Statement of Problem

Study of the chemical and petrologic characteristics of chondritic meteorites has historically received much attention, but very little research on their fabrics has been performed. The deformational histories of asteroidal bodies can only be estimated from study of chondrite microfabrics.

Ordinary chondrites, the focus of this study, are composed of chondrules, matrix, and metal grains. Chondrules are millimeter-sized spherules composed primarily of silicates, usually olivine and pyroxene, and glass; and these objects show evidence for formation as molten droplets. Matrix refers to material that consists of fine-grained silicates, sulfides, graphite, and other components. Iron-nickel metal grains range from spheroidal to ameboidal-shaped and occur as inter-chondrule material or as chondrule rims.

Physical processing of ordinary chondrites has been observed previously in the form of brecciation and optically recognizable shock features. Chondrule- and metal-defined foliations may also be the products of deformation. Quantification of deformation necessary to produce these foliations in chondrites should provide two independent measures of strain; however, the chondrule-strain and magnetic anisotropy measurements have not been quantified or correlated previously within a single chondritic sample. The only quantitative measurements of these two foliations in the same samples have been performed by Kligfield et al. (1982) for terrestrial rocks. For the first time, three-dimensional analyses of strain in chondrules and magnetic susceptibility have been performed in the same chondritic samples. Chondrites are appropriate materials for such an analysis because chondrules can be used as strain markers, due to their presumed initial spherical shapes (Martin et al., 1976).

Chondrule deformation has been quantified in fifteen ordinary chondrites by computerized strain analysis techniques. Separate measurements of magnetic anisotropy were performed by Sugiura and Strangway (1986) in eight samples to quantitatively determine the relative magnitudes and orientations of the principal axes of the susceptibility ellipsoids. The type of petrofabric (foliation vs. lineation) can be defined for each sample based on the shapes of the strain and susceptibility ellipsoids.

Three aspects of the two petrofabrics defined by strain and magnetic anisotropies are discussed in this study. First, the frequency and pervasiveness of fabrics in ordinary chondrites will be discussed. Second, magnitudes and orientations of chondrule strain and magnetic anisotropy will be correlated, and third, the relationship between deformational and petrologic characteristics will be explored to determine whether the foliations were metamorphically or deformationally induced.

Previous Work

Anisotropies have been previously described in chondrites by measurement of magnetic susceptibility in bulk samples, and by microscopic analysis of chondrule shape and alignment. These measurements of chondrule shapes and orientations produced only qualitative descriptions of the petrofabrics. Dodd (1965) examined twenty ordinary chondrites and described a gradation in preferred alignment of elongate chondrule axes. The anisotropy noted did not, however, systematically change with thermal history. Based on these observations, Dodd (1965) postulated that the foliations were not due to metamorphism, but must be a relict depositional feature imposed during accretion of the chondrules. Martin et al. (1975, 1976, 1978, 1980) also performed various two-dimensional analyses of chondrule-defined foliations in chondrites. They believed that the correlation of fabric orientation with chondrule shape resulted from compaction due to overburden pressure in the meteorite parent body.

Cain et al. (1986) performed an extensive analysis of the shape and orientation of chondrules in the Leoville carbonaceous chondrite. They postulated that chondrule shape and alignment resulted from deformation in situ, due to accretionary overburden.

Another fabric in ordinary chondrites, defined primarily by the shape and orientation of metal grains, is reflected in anisotropy of magnetic susceptibility. The magnetic anisotropies and porosities of eight chondritic meteorites were first measured in one plane by Stacey et al. (1961). Porosity was noted to be inversely proportional to magnetic anisotropy. The correlation between metal grain anisotropy and degree of compaction as a function of porosity led to the hypothesis that deformation and volume reduction were principally a result of overburden pressure within the parent body. Weaving (1962) performed a three-dimensional analysis of magnetic susceptibility anisotropies in several chondrites and discovered that each sample could be described by a susceptibity ellipsoid whose shape described the type of petrofabric in each meteorite.

Links between petrographic anisotropy observations (Dodd, 1965; Martin et al., 1975; Martin et al., 1980) and magnetic anisotropies have recently been recognized (Brecher, 1977; Hamano et al., 1982; Sugiura et al., 1983) but not quantified. Hamano et al. (1982) and Sugiura et al. (1983) independently reported a foliation type of magnetic anisotropy for several chondrites, and inferred from the shape of the susceptibility ellipsoids that uniaxial compression was responsible for the anisotropy. Both sets of data supported Dodd's (1965) observation that degree of anisotropy did not correlate with the thermal history of chondrites. Based on their measurements, Hamano et al. (1982) and Sugiura et al. (1983) both proposed that dynamic compression (shock-impact) during initial accretion of the parent body was the dominant orienting mechanism for the metal grains.

II. PETROLOGY OF CHONDRITES

Review of Ordinary Chondrites

Ordinary chondrites are chemically most analogous to ultramafic terrestrial rocks (i.e., peridotites). They vary mineralogically with the degree of thermal metamorphism experienced. Olivine is the most abundant mineral in all ordinary chondrites. Clinoenstatite and calcic orthopyroxene vary in presence and abundance with degree of metamorphism. Plagioclase, which crystallized from glass during metamorphism, ranges in grain size from microcrystalline to coarse. Opaque phases include sulfides, oxides, and Fe-Ni metals.

Matrix and chondrules are the main textural constituents of ordinary chondrites. Two separate types of matrix, based on chemical differences, have been observed in ordinary chondrites: a fine-grained silicate or "Huss" matrix (Huss et al., 1981), and a graphite-magnetite matrix (Scott et al., 1981). Chondrules in ordinary chondrites have been classified according to different textural characteristics as porphyritic and nonporphyritic (Gooding and Keil, 1980).

The classification of ordinary chondrites is based on chemical and metamorphic variations. All have very similar Mg/Si ratios, but vary in total Fe content and oxidation state (reflected in the distribution of Fe between silicates and metal). The ordinary chondrites are subdivided into three compositional groups: H, L and LL. The metal-silicate fractionation responsible for these samples must have occurred prior to or during their accretion.

Ordinary chondrites also display a variation in degree of textural integration. Some samples have diffuse chondrule boundaries, indistinguishable from an overall granular texture, whereas others have distinct chondrule perimeters in a fine-grained matrix. Degree of textural integration parallels mineralogical variations such as increasing homogeneity of olivine and pyroxene, and recrystallization of glass to form plagioclase. Van Schmus and Wood (1967) proposed a petrologic sequence for chondrites based on these textural and mineralogical variations. Ordinary chondrites are therefore described in terms of four petrologic types, (representing the degree of thermal metamorphism experienced) : 3, 4, 5, and 6. Type 3 is the most primitive and unequilibrated type, whereas Type 6 is the most equilibrated and recrystallized. By ammending appropriate petrologic types to H, L, and LL chondrites, Van Schmus and Wood (1967) thus defined the two-fold classification presently in use.

Ordinary chondrites have been physically as well as petrologically processed. Dodd and Jarosewich (1979) developed a classification for equilibrated chondrites based on petrographic observations of shock features. Six classes, a-f, describe increasing intensity of shock.

The three chemical groups of ordinary chondrites, H, L and LL, are commonly believed to represent distinct asteroidal parent body types. Genomict breccias consist of fragments of different petrologic type but of the same chemical group. The preponderance of these genomict breccias in ordinary chondrites indicates that there was very little, if any, mixing among the groups during brecciation (Rubin et al., 1983). This observation supports the hypothesis that different classes of ordinary chondrites originated on separate parent bodies, and that these contained a range of petrologic types formed by thermal metamorphism.

Petrographic Description of Samples

Fifteen ordinary chondrites of Types 3 and 4 and one of Type 5 were obtained from various museums for this study (Table 1). Samples of low petrologic type were selected because chondrites that have experienced extensive textural integration make petrofabric analyses of this type impossible. In the strain analysis techniques utilized, unacceptable errors are introduced if chondrule perimeters can not be easily distinguished and accurately traced. In the following section, mineralogy, chondrule textures and structural features are considered.

Mineralogy

Olivine is the most common mineral and occurs in chondrules and as individual grains in matrix. Most grains are euhedral and have a bimodal range in size of 0.01mm to 0.05mm in porphyritic chondrules and 0.1mm to 0.5mm as phenocrysts in porphyritic and barred chondrules. Ortho- and clinoenstatite occur as long, tabular grains and polysynthetically twinned needle-like grains, respectively. Clinoenstatite commonly encloses euhedral olivine phenocrysts or is intergrown with orthopyroxene. Troilite occurs as large, irregularly shaped grains in the matrix, and as small equant grains within and rimming chondrules and metals. Chromite, the predoeinant oxide, occurs as blebs enclosed by troilite. Fe-Ni metal grains (kamacite and taenite) range from spherical to ameboidal in shape. They display a wide variation in size but are commonly distributed between chondrules

Table 1. List of meteorites used in this study.

Meteorite	Classification	Source *	Best Descriptive Reference
1. Mezo-Madaras (H)	L3	HMM	Dodd et al., 1965a
2. Mezo-Madaras (S)	L3	SNMNH	Dodd et al., 1965a
3. McKinney	L4	FMNH	Mason, 1963a
4. Barratta	L4	FMNH	Dodd et al., 1967a
5. Farmington	L5	FMNH	Keil et al., 1964a
6. Broken Bow	H4	ASU	Mason, 1963a
7. Parnallee	LL3	AMNH	Dodd et al., 1967a
8. Menow	H4	HMM	Keil et al., 1964a
9. Kesen	H4	HMN	Keil et al., 1964a
10. Grady	H3	ASU	Van Schmus et al., 1967a
11. Ankober	H4	SNMNH	Mason, 1967a
12. Clovis	H3	SNMNH	Dodd et al., 1967a
13. Faucett	H4	UCLA	Mason, 1967a
14. Hammond Downs	H4	SNMNH	Mason, 1973a
15. Adrian	H4	ASU	Mason, 1963a
16. Kelly	LL4	?	Fredriksson et al., 1968a

*

Harvard Mineralogical Museum (HMM)
Smithsonian National Museum of Natural History (SNMNH)
Field Museum of Natural History (FMNH)
Arizona State University (ASU)
American Museum of Natural History (AMNH)
University of California, Los Angles (UCLA)

or are found rimming chondrules in a manner similar to troilite.

Chondrule Textures

Ordinary chondrites contain 70 - 85% porphyritic and 15 - 30% nonporphyritic chondrules (Gooding et al., 1980). Porphyritic olivine-pyroxene chondrules are by far the most abundant chondrule type, generally displaying a circular to oblong shape. Whole barred olivine and radial .pa pyroxene chondrules are nearly always spherical; however, many chondrules are broken.

Structural Features

The more highly deformed samples (1-6 in Table 1) show a vague foliation defined by chondrules and metal grains; however, most specimens display no apparent foliations or lineations on visual inspection. Many samples contain lithic breccia clasts composed of broken barred olivine, radial pyroxene, and porphyritic olivine-pyroxene chondrules enclosed in a fine-grained matrix. Other lithic clasts consist entirely of equigranular, equant olivine (olivine microporphyry). The clasts occur in a variety of sizes and shapes and do not appear to display preferred orientation. The unbroken chondrules within the clasts tend to be nearly spherical or very slightly oblong.

Veins cut through almost every sample in random criss-crossing networks. The individual veins vary in width (0.02mm to 0.1mm) and pass through chondrules and matrix. The veins ,composed predominantly of hematite, are presumably terrestrial weathering features

Brecciation

A brief review of brecciation is presented, because of its potential significance in determining deformation mechanisms. The general abundance of H, L and LL genomict breccias were determined by Binns (1967) as 25%, 10% and 62%, respectively. However, it has recently become evident that almost all ordinary chondrites are probably fragmental genomict breccias at some scale (Keil, 1982). Samples from this study that have been described as fragmental breccias are McKinney, Barratta, and Grady (Rubin et al., 1983), Kelly (Bunch and Stoffler, 1974), and Mezo-Madaras (Van Schmus, 1967). Rubin et al. (1983) speculated that the high proportion of genomict breccias documented by Binns (1967) and Keil (1982) may have resulted from several episodes of parent body disruption and reassembly after metamorphism had produced the different petrologic types.

The breccias observed in this study contain relatively few clasts and average from 1-2 centimeters in diameter. Breccia clasts that are large enough to constitute the entire cubic sample from which the thin sections are made have not been found. The breccia clasts observed in this study are minor parts of each sample; therefore, dominant fabrics defined by chondrules in the host are not obscured during brecciation and thus, can be measured.

III. MEASUREMENTS OF STRAIN IN CHONDRITES

Chondrule Strain Analysis

Strain measures the changes in lengths, angles, or relative dimensions. Strain markers are needed to record the changes in shapes, line lengths, or angles (Lisle, 1985). Strain measurement involves comparison of the initial shapes of strain markers with their deformed states. Strain is usually expressed in three-dimensions by a strain ellipsoid. Strains are classified according to the change in the strain ellipsoids shape from its inferred prestrained shape (Means, 1976).

Observations

The four strain analysis techniques used in this study are extensively described in Appendix I. Chondrites are appropriate materials for strain analysis because chondrules can be used as strain markers, due to their presumed initially spherical shape (Martin et al., 1976). Lithic clasts from brecciated meteorites and broken chondrules were omitted from the analysis.

When determining the total strain in chondrites, the shape and orientation of the deformed chondrules do not necessarily represent the shape and orientation of the strain ellipsoid in the chondrite. Several factors may influence a chondrule's final shape and orientation, including the chondrule's initial shape and orientation and the strain intensity and orientation. Total strain may also include matrix strains which are not reflected in chondrules at all.

Fifteen ordinary chondritic samples have been examined for deformation by measuring two-dimensional strain on three orthogonal faces for each sample. To determine the amount of shape change that the chondrules underwent, maximum and minimum dimensions of chondrules on each face were measured to obtain deformed particle axial ratios (Rfinal). Ø, the angular orientation of the maximum Rf axes with respect to an arbitrary reference line was also measured (ELLIPSE-TRACING program, Appendix I). By tracing the perimeters of individual chondrules, values of Rf and Ø were measured and plotted on an Rf/Ø graph for three faces on each sample (Rf/Ø Program, Appendix I). These graphs enable the determination of axial ratios of the mean finite strain ellipse (Rs) imposed on each face. The symmetrical distribution of data points in four quadrants is defined by the hyperbolic function curve whose minimum point of curvature is Rs (Figs. 1 and 2). The greatest degree of symmetry is used as a guide in determining the finite strain ellipse ratio (Rs)(Dunnet, 1969).

From the fifteen chondrites analyzed for strain, the meteorites Mezo-Madaras and McKinney represent the maximum deformation and Adrian and Kelly represent the minimum deformation as indicated by Rs values (Figs. 1 and 2). Mezo-Madaras exhibits the largest strain (Rs) and the most pronounced foliation. Rf/Ø plots for all three faces (Fig. 1a-c) display a general clustering of data points around a maximum Rf over a small range of fluctuation (Ø), indicating a strong preferred orientation of chondrules. The aspect ratio of 1.39:1 measured on the ca face, is the greatest deformation recorded in any of the samples. McKinney (Fig. 1d-f) is the second most deformed sample in the group of chondrites measured. Values of Rs ranging from 1.34:1 to 1.11:1 and the

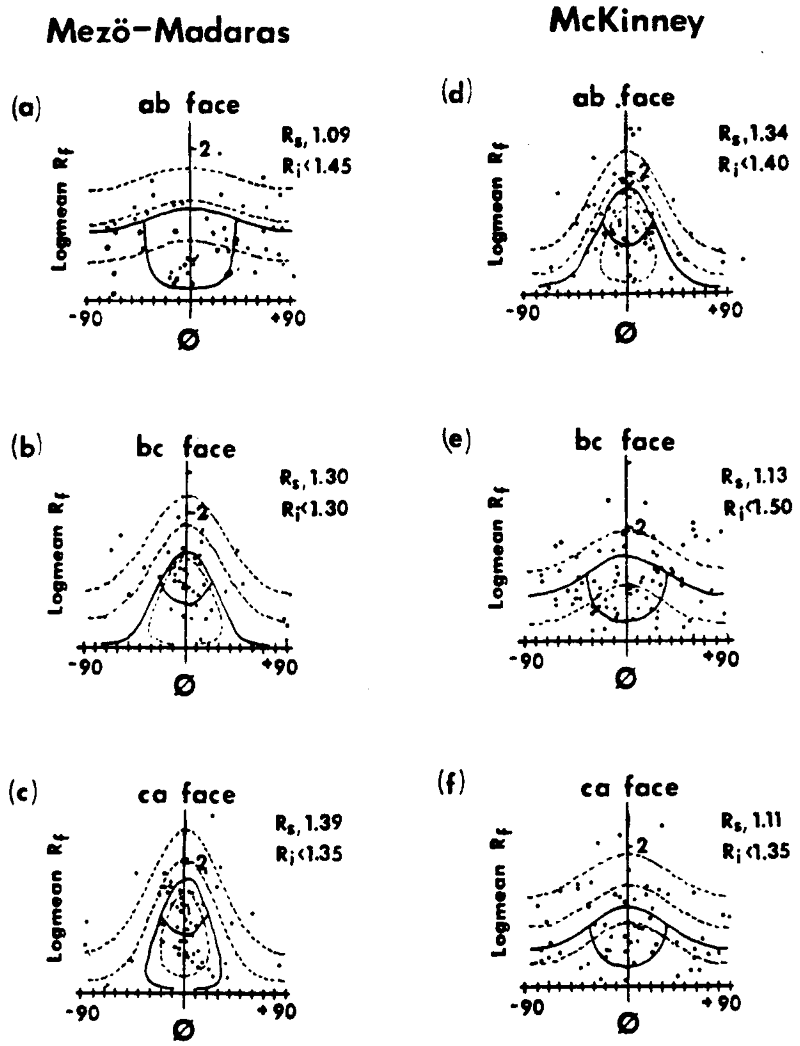

Figure 1. Rf/Ø graphs for the three orthogonal faces measured for Mezo-Madaras (H) and McKinney are displayed. The smallest Ri of 1.25:1 is indicated by the inner most dotted Rf/Ø curve, the largest Ri of 1.75:1 is represented by the outer most dotted curve, the middle dotted curve corresponds to an Ri of 1.5:1 and the solid curve indicates the best fit mean Ri for the data. (a) Rf/Ø curve displays very low strain with a weak preferred orientation of chondrules; (b and c) Rf/Ø curves display moderate strain with a preferred orientation that is well pronounced; (d) Rf/Ø curves display moderate strain with a preferred orientation of chondrules that is well defined; (e and f) Rf/Ø curves display low strains with weak preferred orientation of chondrules.

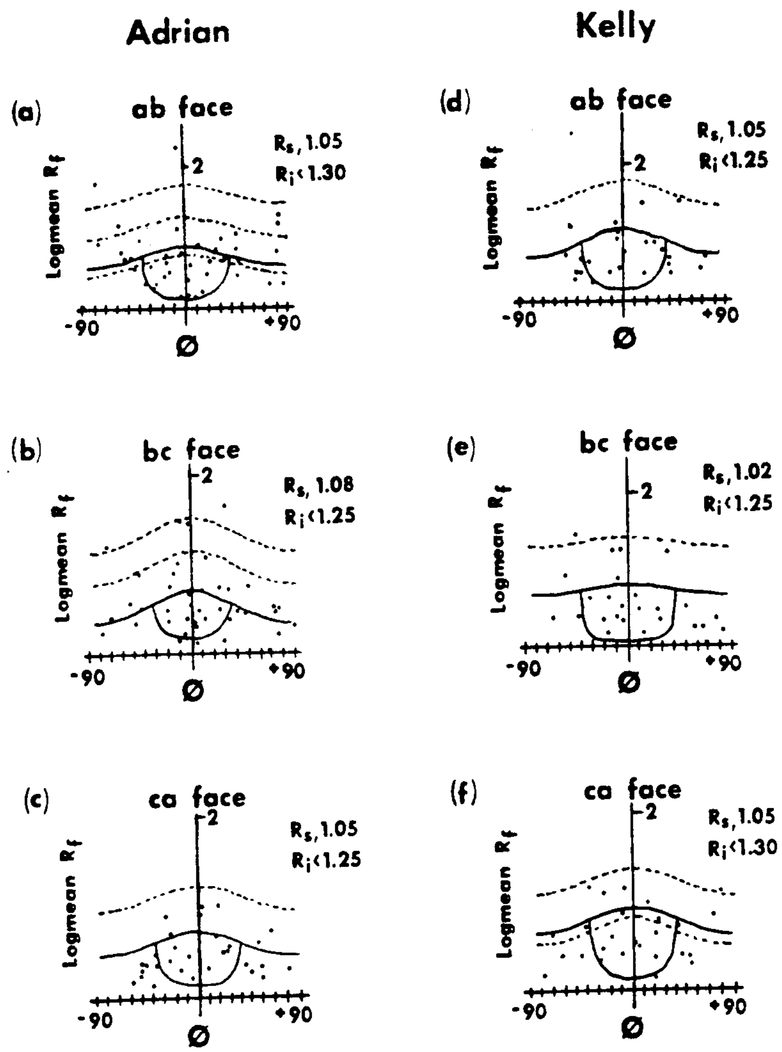

Figure 2. Rf/Ø graphs for the three orthogonal faces measured for Adrian (a-c) and Kelly (d-f). Rf/Ø curves display very low strains with weak preferred orientation of chondrules for each face of both samples.

preferred orientation of chondrules indicate that this sample has been deformed as well.

In contrast, Adrian and Kelly exhibit the least amount of strain. All three Rf/Ø plots for Kelly (Fig. 2a-c) and Adrian (Fig. 2d-f) display a large fluctuation of Ø and a lack of data points clustering at a maximum Rf. This type of broad scatter of points of low Rf value shows that the chondrules in Kelly and Adrian have very little preferred orientation. The low Rs values range in Adrian from 1.05:1 to 1.08:1 and range in Kelly from 1.02:1 to 1.05:1, indicating a lack of penetrative deformation. Rf/Ø data for these four samples (Mezo-Madaras, McKinney, Adrian, and Kelly) are listed in Appendix I, Rf/Ø Data. Rf/Ø graphs for the twelve samples whose Rs values fall in between the range of deformation discussed are presented in Appendix II.

Spherically shaped chondrules have been defined as those whose axial ratios b/a and c/b were less than 1.5:1 (Martin, 1976). 98% of the 342 chondrules measured by Martin (1976) fall into this "spherical class". Although the assumption of initial sphericity is made for the chondrules in this study to qualify them as strain markers, this assumption must be tested to allow a more lucid interpretation of the low Rs values calculated.

It is critical to determine whether the finite strain ellipse (Rs) previously calculated has a higher or lower ellipticity than the initial shapes of chondrules. A relationship therefore can be determined between the final strain than the initial shapes of chondrules. A relationship therefore can be determined between the final strain ratio and orientation of chondrules (Rf and ϕ) and their intial shape and orientation (Ri and θ). A progression of emperically derived Rf/ϕ curves (Dunnet, 1969) are generated for individual Rs values for each sample face. The curvature of the Rf/ϕ curves is a function of Rs, therefore, a set of Rf/ϕ curves are uniquely generated for each Rs value. Each Rf/ϕ curve encloses values of Ri which progressively increase as the different Rf/ϕ curves move up the Rf axis. By superimposing Rf/ϕ curves on the Rf/ϕ data, an approximate mean ratio of initial shape (Ri) can be determined from the curve that qualitatively best fits the data.

Four Rf/ϕ curves have been superimposed on the plotted Rf/ϕ data for each sample face (Figs. 1 and 2). The smallest Ri of 1.25:1 is indicated by the innermost dotted Rf/ϕ curve, the largest Ri of 1.75:1 is represented by the outermost dotted curve, the middle dotted curve corresponds to an Ri of 1.5:1, and the solid curve indicates the best fit mean Ri for the data. In cases where the mean Ri for the sample corresponds with one of the dotted curves, the solid curve is superimposed on that dotted curve. Values of Ri greater than Rs are indicated when the best fit curve is open and fluctuation (ϕ) is greater than 90 . When Rf/ϕ curves that best fit the data are closed, Rs values exceed those of Ri.

A set of Rf/ϕ curves were superimposed on the endmember samples, Mezo-Madaras, McKinney, Adrian, and Kelly. Values of Ri range from less than 1.30:1 to less than 1.50:1 in the samples with higher Rs values (Mezo-Madaras and Mckinney). Ri ranges from less than 1.25:1 to less than 1.30:1 on the samples with lower Rs values (Adrian and Kelly)

(Figs. 1 and 2). All other plotted Rf/ϕ data have Rf/ϕ curves superimposed and are presented in Appendix II.

The only face from every sample in which Rs exceeds Ri is the ca face of Mezo-Madaras (Fig. 1c). The data are best fit with a closed Rf/ϕ curve and the amplitude of the other superimposed Rf/ϕ curves is very high. The high amplitude of these curves indicates that data are clustering at a maximum Rf across a small range of fluctuation; therefore, higher amplitude curves describe more strongly pronounced preferred orientations of chondrules. The data on every other face however, are best fit with open ended Rf/ϕ curves varying in amplitude with degree of preferred orientation.

Exclusive analysis of the very low magnitude of strain measured compared to the higher values of initial shape, leads to suspicion of the small finite strain values. The question arises as to whether chondrites really have been deformed or if only the initial ellipticity of chondrules is being measured. Despite the low magnitude of the finite strains measured, the geometry of the high amplitude curves along with the symmetrical distribution of data along the fluctuation (ϕ) scale, indicates a deformationally induced preferred orientation of chondrules.

To some extent the choice of Rs is subjective and relies on a visual best fit. As an independent internal check on the choice of Rs from Rf/ϕ data, the reciprocal strain ellipse or "destraining ellipse" was fitted for each sample face, using computerized methods described by Peach and Lisle (1979) (THETA Program, Appendix I). Each sample was successively destrained by superimposing a reciprocal strain ellipse

(R(s)) on each deformed chondrule (Rf/ϕ). The direction perpendicular to the maximum chondrule axes was used as the destraining direction. To destrain each chondrule, the reciprocal strain ellipse was altered incrementally until the most isotropic distribution of chondrule maximum axes was achieved. After destraining, the chi-square statistical test was applied to check the hypothesis that the mean predeformational orientation of the long axis (theta) calculated for each face represented a sample from a population of chondrules with an isotropic orientation.

In samples of low strain, ϕ is difficult to define accurately because the deformed particle shapes are only slightly different from a circle. Because it is from the most isotropic orientation that the destraining value of Rs is determined, the destraining analysis has been recommended only as a check for samples with strains greater than Rs = 3.0 (Borrdaile, 1984). Despite the fact that the greatest strain measured on any of the samples in this study was Rs = 1.39, the destraining method tested for applicability.

The statistical chi-square test applied to Mezo-Madaras, McKinney, Adrian, and Kelly (Figs. 3 and 4), involves the division of theta values for each chondrule into classes of similarity defined by a progression of Theta curves. A graph of chi-square vs. reciprocal strain ellipse (R(s)) is generated for each face, allowing the goodness of fit of the theta curves to the data to be evaluated. In each face of Mezo-Madaras, McKinney, Adrian, and Kelly, the lowest chi-square value exists beyond the 5% significance level (denoted by the dashed line), indicating that the corresponding destraining ellipse (R(s)) may be

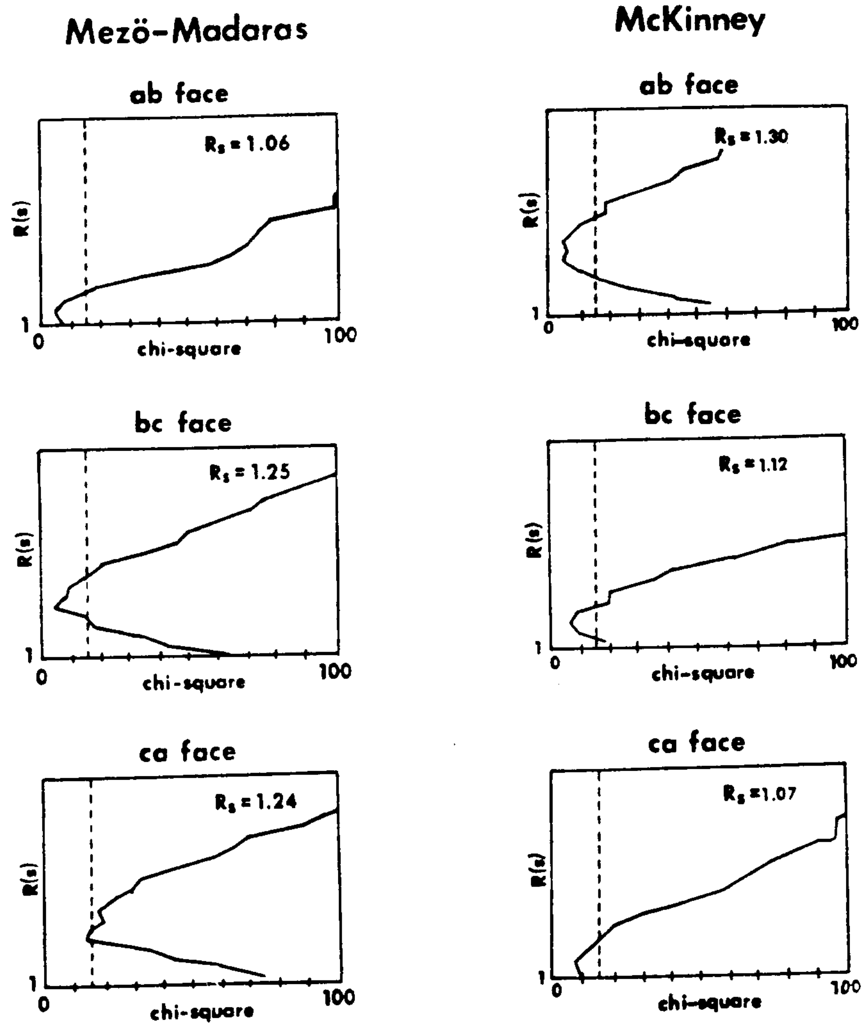

Figure 3. Chi-square vs. reciprocal strain ellipse graph for the three orthogonal faces measured for Mezo-Madaras and McKinney. All curves extend beyond the 5% significance level (dashed line) indicating validity of the Theta program as an independent internal check on Rf/Ø data for these samples. The maximum point of the curve extending beyond the 5% significance line corresponds to the mean reciprocal strain ellipse for that face.

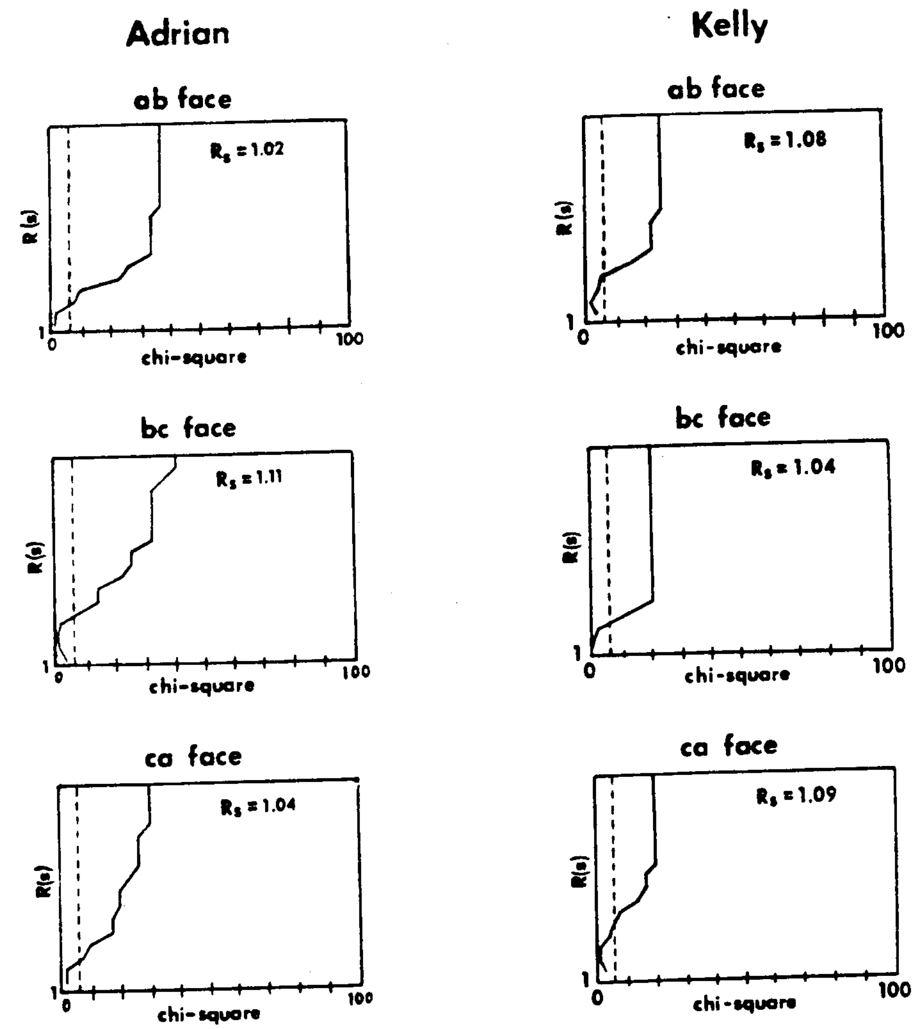

Figure 4. Chi-square vs. reciprocal strain ellipse graph for the three orthogonal faces measured for Adrian and Kelly. All curves extend beyond the 5% significance level.

taken to be the axial ratio of the provisional strain ellipse. Destraining ratios statistically determined for each face of the four samples presented nearly approximate Rs values for each sample from Rf/Ø data (as shown by correlation coefficients in Appendix II, Table 7). This objective test thus validates the more subjective determination of Rs from Rf/Ø data.

Axial ratios, representing values of Ri, were also measured for the chondrules in their statistically most isotropic orientation. The arithmetic mean Ri for each face in its destrained state displays a good correlation with Ri values determined from the visual best fit of Rf/Ø curves superimposed on the deformed data (as shown by correlation coefficients in Appendix II, Table 7)

In light of these observations, the initial shape of chondrules can be described more precisely as being subelliptical. In addition, adherence to Martin's (1976) definition of a sphere (axial ratios of 1.5:1) would cause minor amounts of deformation in chondrites (like that described in the samples from this study where Rs ranges from 1.02:1 to 1.39:1) to be overlooked.

After a two-dimensional strain ellipse has been measured on each orthogonal face, the three-dimensional strain ellipsoid for each sample can be determined. Using the axial ratio and orientation of the two-dimensional strain ellipse from each face, a computerized series of three by three matrix transformations was used to calculate the axial ratios and true orientations of the principal planes of the three-dimensional strain ellipsoid (PASE 5 Program, Appendix I). The shapes of the strain ellipsoids measured for the fifteen samples are qualitatively depicted on a Flinn diagram (Fig. 5). The type of deformation, constrictional or flattening, experienced by each ellipsoid may be determined from its position relative to the plane strain line (K=1). Figure 5 also enables a qualitative determination of the amount and gradation of deformation from the distance each ellipsoid plots from the coordinates (1,1). All samples cluster near the origin of the diagram, graphically depicting the low amount of deformation experienced. The relatively higher strained samples samples, representing a gradation in deformation of 8-17% shortening, all plot within the "flattening-type" deformation field, indicating deformation by shortening along the principal minimum axes (c). Samples with deformation of 7% or less plot near the plane strain line or just within the "constrictional-type" deformation field. Table 2 lists the axial ratios for each three-dimensional ellipsoid generated and their corresponding percent flattening along the minimum principal axis (c).

A three-dimensional analysis of each sample was also made, using the reciprocal strain ellipse ratios (R(s)) generated from the destrained state, to calculate the reciprocal strain ellipsoid. Axial magnitudes and percent flattening of the destrained ellipsoids (calculated from theta data) correlate with those of the deformed ellipsoids (calculated from Rf/Ø data) for all samples within analytical error (Table 2). The reciprocal strain ellipsoid has a greater degree of flattening in twelve of the fourteen samples, so the mean strain ellipsoids used in this study may be conservative estieates. Although Borrdaile (1984) questions the reliabilty of data acquired from the destraining method of strain analysis for samples of

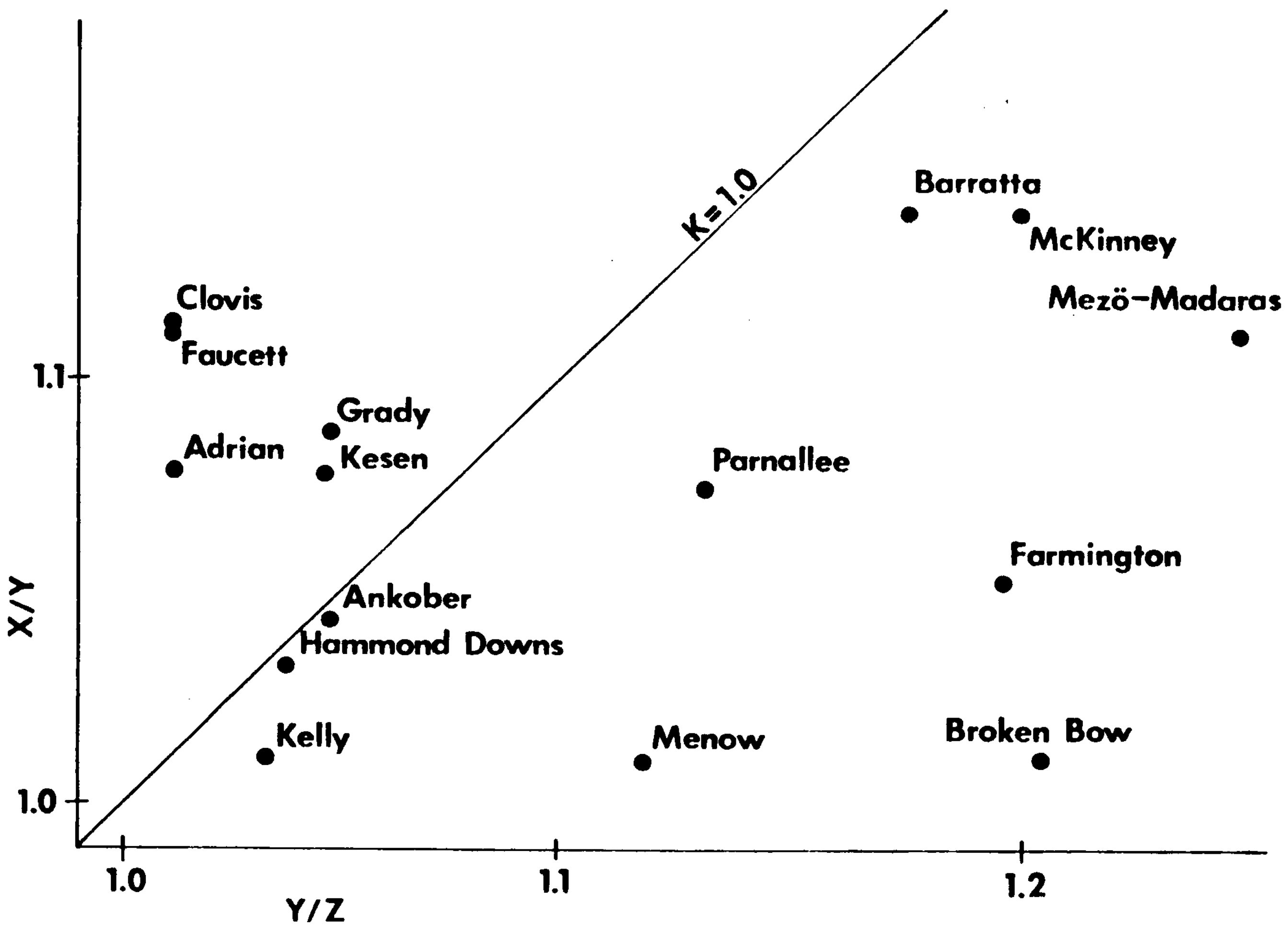

Figure 5. Flinn diagram plotting all mean strain ellipsoids. Type of stress regime (flattening vs. constrictional) experienced by each sample is indicated by the position the sample plots relative to the plane strain (K=1) line. The parameters X, Y and Z are described by the maximum, intermediate and minimum lengths of an ellipsoid, respectively.

Table 2. Axial magnitudes and percent flattening of mean strain and reciprocal strain ellipsoids.

Meteorite	Rf/O a	Rf/O b	Rf/O c	Rf/O % Flattening	Theta Data a	Theta Data b	Theta Data c	Theta Data % Flattening
Mezo-Madaras (H)	1.18	1.03	0.82	17.57	1.12	1.03	0.87	12.98
Mezo-Madaras (S)	1.13	1.05	0.85	15.43	1.13	1.05	0.85	15.43
McKinney	1.16	1.02	0.85	14.72	1.13	1.01	0.87	12.84
Barratta	1.15	1.01	0.86	14.49				
Farmington	1.10	1.04	0.87	12.70	1.11	1.04	0.87	13.42
Broken Bow	1.08	1.06	0.88	12.31	1.07	1.03	0.91	9.39
Parnallee	1.10	1.02	0.90	10.44	1.10	1.00	0.91	8.97
Menow	1.05	1.03	0.92	8.02	1.06	1.03	0.92	8.31
Kesen	1.07	0.99	0.94	6.17	1.09	1.00	0.92	7.84
Grady	1.08	0.99	0.94	6.08	1.07	0.99	0.94	6.14
Ankober	1.05	1.00	0.95	5.04	1.06	1.00	0.95	5.33
Clovis	1.08	0.97	0.95	4.71	1.08	0.97	0.95	4.71
Faucett	1.08	0.97	0.95	4.57				
Hammond Downs	1.04	1.00	0.96	4.50	1.04	1.00	0.96	4.50
Adrian	1.06	0.98	0.96	3.68	1.06	0.99	0.95	4.71
Kelly	1.03	1.01	0.97	3.12	1.04	1.01	0.95	4.92

low strain, this exercise demonstrates that the analysis in this case is consistent with other methods, even for low strains, because the destraining ratio (Rs) and initial shape ratio (Ri) values and reciprocal strain ellipsoids generally correlate with those from Rf/Ø data.

To determine the degree of analytical error involved in this analysis, the same computerized strain analysis methods were used on perfect spheres traced from a template. A strain ellipsoid was generated with relative magnitudes of the principal axes being a = 0.96; b = 0.97; and c = 1.07, amounting to a 4% shortening along the principal minimum axis. The shape of this ellipsoid plots in the "constrictional-type" deformation field on a Flinn diagram. Because the minimally strained samples generally are described by the same ellipsoidal shape as the sphere measured in the experiment, samples that fall within this analytical error are assumed to be essentially undeformed.

Other experiments tested reproducibility of digitizing the same chondrules and achieving similar results (ELLIPSE-TRACING program, Appendix I). In the first experiment, the photographs from which initial measurements were made were remeasured for one highly strained and one low strained sample. The new results were within 4% of the first measurements, thus supporting reproducibility of data. Another experiment involved testing reproducibility of results on two different samples of the same meteorite. One cube of Mezo-Madaras (H) was obtained from Harvard University and a second was obtained from the Smithsonian Institution (S). Axial ratios for the mean strain ellipsoids for both samples describe "flattening-type" spheroids. The percent flattening fell within analytical error (Table 2).

The 4% absolute analytical error involved in the chondrule measurements may be accounted for in several ways. The most obvious cause for error in the chondrule measurment is operator error. The fairly wide spacing of the grids on the digitizing tablet used leads to degradation in reproducibility. A fair amount of bias may be involved as well, because the operator selects each object to be measured in the ELLIPSE-TRACING program. All subsequent determinations of deformation, subjective or objective, are drawn from the ELLIPSE-TRACING data set, thus perpetuating possible operator error. Another potential error is involved in fitting the Rf/Ø curves to the data. An arbitrary value of 60% of the data points was used to fit each set of data with an Rf/Ø curve. A method for determining the statistical errors involved in the subjective choice of these curves unfortunately has not yet been formulated for this strain analysis technique. The most probable cause for error however, is the low amount of strain in the samples. Despite the fact that these are non-spherical particles, the strain analysis techniques used are not sensitive enough in very low-strain data sets to distinguish true deformation.

Magnetic Anisotropy

Methods of Magnetic Measurements

All magnetic susceptibility anisotropy measurements were made by N. Sugiura and D.W. Strangway at the University of Toronto. The magnetic anisotropies were measured on the same cubic samples used for the strain analysis with a Princeton Applied Research spinner magnetometer. Bulk initial susceptibility was measured with a vibrating sample magnetometer designed for small samples. From the data on bulk and anisotropic susceptibility, susceptibility tensors were calculated. Three principal components of intrinsic magnetic susceptibilities and their orientations relative to the coordinate system used for strain analysis measurements were also calculated. A +/-3% relative analytical error was determined based on the effects of irregular sample shape and error in the bulk susceptibility measurement. The procedures employed are described in detail by Sugiura et al. (1983).

Observations

Magnetic susceptibilities were measured in eight of the fifteen samples analyzed for strain. Maximum, minimum, and intermediate axial magnitudes of the three principal axes of the susceptibility ellipsoids are listed in Table 3. A gradation in anisotropy is evident, with Barratta and Kelly bracketing the range of deformation. The magnetic susceptibility ellipsoid for each sample is described by a "flattening-type" spheroid. Such susceptibility ellipsoids indicate progressive foliation development and therefore deformation by shortening along the minimum principal axes (X1).

Table 3. Principle axes of magnetic susceptibility ellipsoids.

Meteorite	X1 *	X2 *	X3 *
Barratta	0.006550	0.010010	0.010360
McKinney	0.005090	0.007200	0.007570
Broken Bow	0.013180	0.018850	0.019320
Parnallee	0.001910	0.002780	0.002870
Grady	0.017530	0.023700	0.024260
Faucett	0.012690	0.015820	0.016580
Adrian	0.006080	0.006550	0.006790
Kelly	0.000515	0.000544	0.000565

* = emu/gOe

Comparison of Fabrics

Ellipsoid Axial Magnitudes

To facilitate correlations in magnitude of deformation, strain ellipsoid axial ratios and susceptibility ellipsoid axial magnitudes were plotted in Figure 6. The parameters R1, representing intensity of deformation, and R2, representing dominant type of anisotropy, were plotted for all meteorites for which magnetic and strain measurements were made. Magnitudes of the three principal axes of the susceptibility ellipsoids were used to determine R1 and R2 values for the eight samples measured. R1 and R2 were also calculated, using the principal axial ratios generated for the mean strain ellipsoids that had magnetic measurements. The two possible types of anisotropy, foliation and lineation, are defined by oblate or flattening-type and prolate or constrictional-type spheroids, respectively. The amount that each sample deviates to the right of the pure foliation curve indicates the relative magnitude of lineation in the samples.

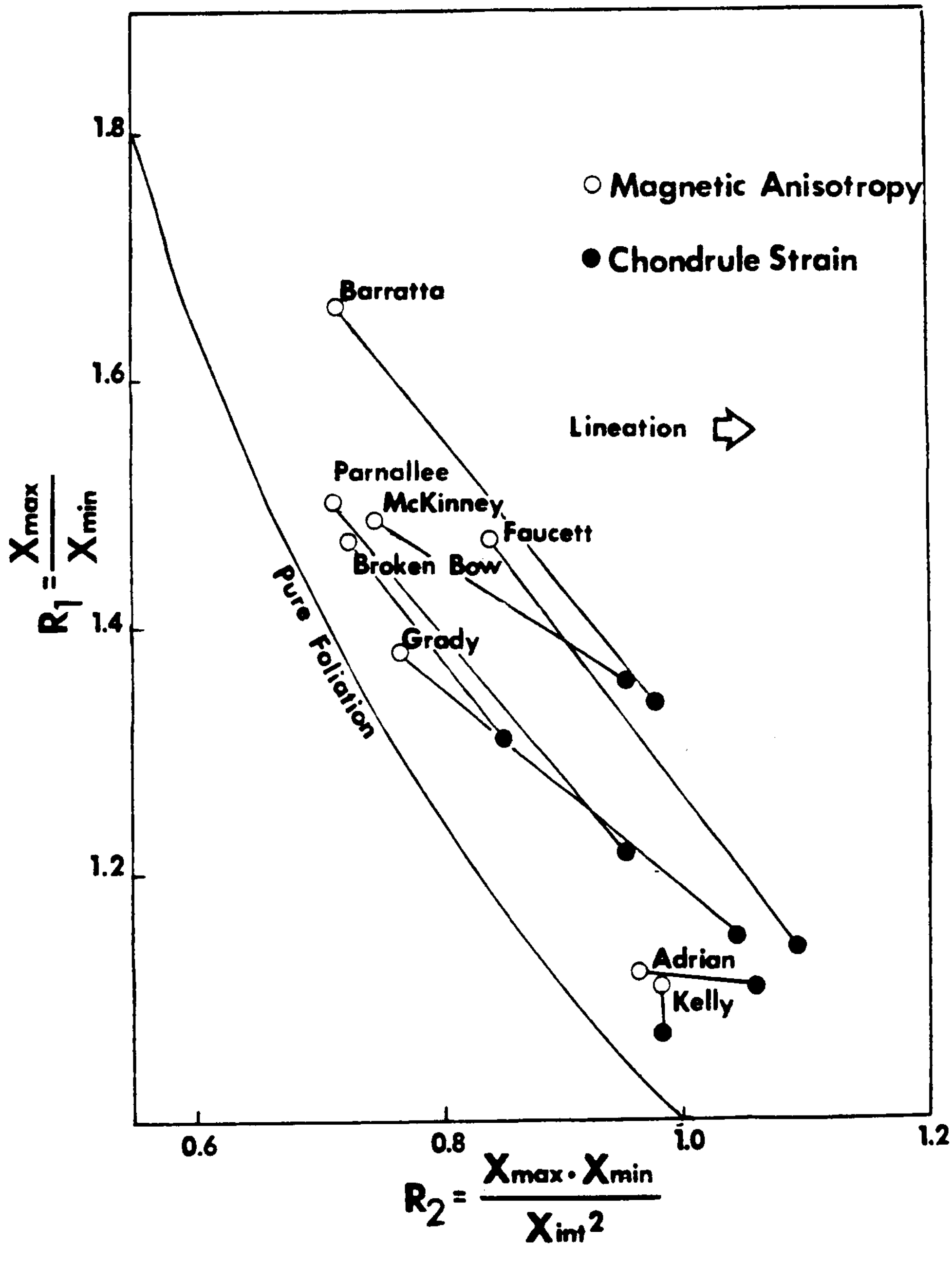

Figure 6. Shape (R_2) vs. intensity (R_1) graph comparing gradation in relative intensity of foliation developement with respect to the shape of each ellipsoid for both chondrule-strain and magnetic susceptibility measurements.

As the two different sets of strain data are not strictly comparable, an exact agreement between them is not expected. The gradation of intensity (R1), within each data set correlates well. Figure 7 displays the relationship in intensity between R1 magnetic and R1 strain. A linear regression for this relationship is given by:

$$R1 \text{ magnetic} = 1.478 \ R1 \text{ strain} - 0.406, \tag{1}$$

with a regression coefficient of +0.88. From this equation, the relative intensity of the mean strain ellipsoid can be determined from magnetic susceptibility data. This is useful because it is difficult to obtain three orthogonal thin sections of chondrites necessary for strain analysis and the procedure is very time consuming. Magnetic susceptibility is a rapid and non-destructive measurement. By using this relationship between strain and magnetic susceptibility, magnetic susceptibility anisotropies can be used in the future to determine directly the general strained state of ordinary chondrites.

Orientations

The physical orientations of the strain axes are inconsequential to the strain analysis technique because of the arbitrary choice of reference system. The orientation becomes important, though, when the orientation of the magnetic susceptibility ellipsoid an the same sample is compared with the orientation of the strain ellipsoid. Correlations between these data are possible when the same reference system is used for each sample for both measurements.

In addition to correlations between axial magnitudes, orientations

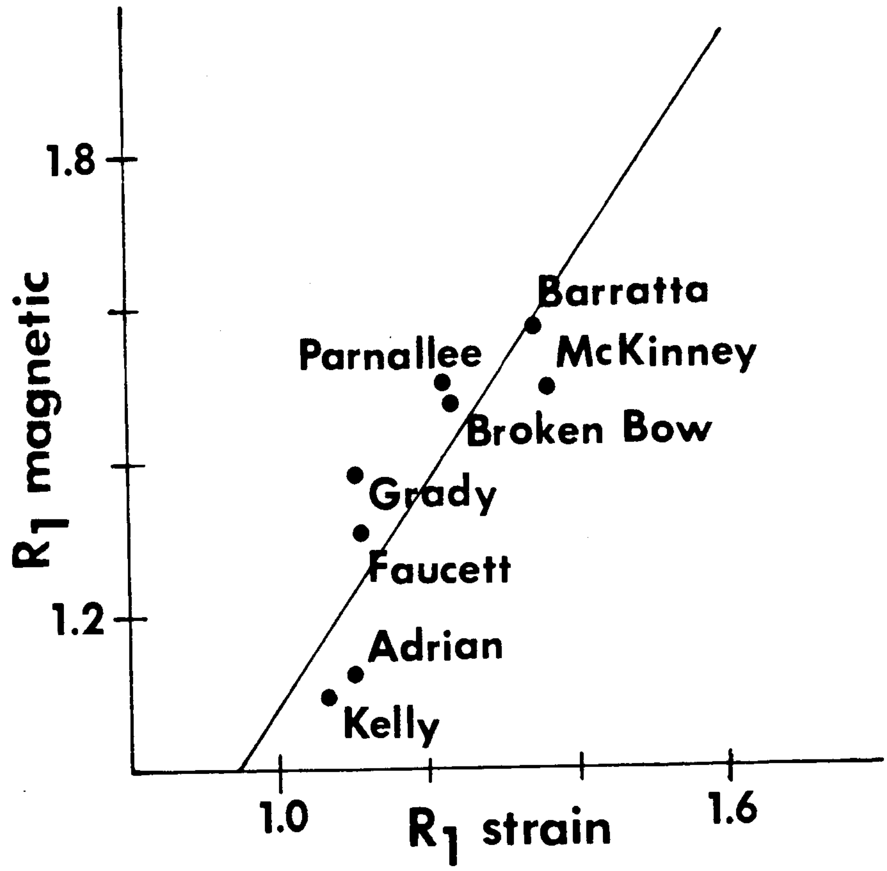

Figure 7. R_1 magnetic vs. R_1 strain graph displaying the relationship in relative intensity of foliation development for the strain and magnetic susceptibility ellipsoids.

of the principal shortening axes of the strain ellipsoids (c) align subparallel to the shortened axes of the magnetic susceptibility ellipsoids (X1) in all samples except for Faucett and Kelly. Orientations of the principal axes of the strain and susceptibility ellipsoids are plotted on equal area stereonets in Figure 8. The angular deviations betweenthe minimum axis of the strain ellipsoid (c) and the minimum axis of the susceptibility ellipsoid (X1) are reported on Table 4. McKinney, Barratta, Parnallee and Adrian show the closest correspondence between all principal axes of both types of ellipsoids: a//X3; b//X2; c//X1. Grady and Broken Bow have the same subparallel correspondence, but the angular deviations between corresponding planes from each ellipsoid are greater.

Kelly and Faucett are the anomalous samples. The correspondence of all principal axes of both ellipsoids differs from all other samples. One possible cause for the discrepancy in orientation is that magnetic anisotropy may be controlled by tetrataenite, which has very strong crystalline anisotropy (N. Suigiura, Per. Comm., 1986). However, Grady and Adrian are H chondrites and probably do not contain large amounts of this metallic phase. Also, a prolate anisotropy is expected if it is due to tetrataenite; thus, the magnetic anisotropy is believed to be determined by shape anisotropy of the kamacite-taenite grains. The lack of correspondence of principal axes thus, are probably due to the low amount of strain measured in these samples.

In samples with low strain, the long axis orientation of individual strain markers may be difficult to define accurately when the deformed particle shape approaches that of a circle; therefore,

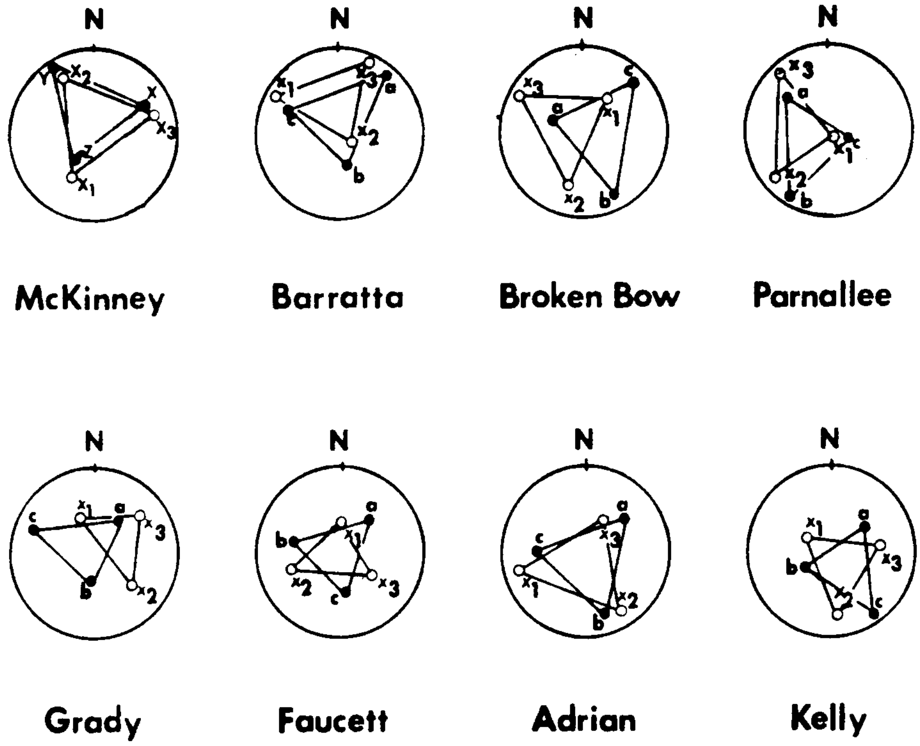

Figure 8. Equal-area stereonets comparing orientation of the principal axes of the mean strain and magnetic susceptibility ellipsoids. All measurements are plotted in the lower hemisphere with the exception of Grady (X_2) and Parnallee (X_3) which are plotted in the upper hemisphere.

Table 4. Angular deviation between strain ellipsoid minimum axis (c) and susceptibility minimum axis (X1).

McKinney	0.20
Barratta	3.32
Broken Bow	37.88
Parnallee	11.76
Grady	32.16
Faucett	4.74
Adrain	13.29
Kelly	28.00

incremental errors in accurate determination of an ellipsoid's long axis could lead to an anomalous mean strain ellipse for each individual face. The orientation of this strain ellipse along with two other orthogonal ellipses is subsequently used to calculate the orientation of the mean strain ellipsoid's principal axes. In samples of very low strain, it is thus easy to visualize an interchange of principal axes.

These strong correlations of axial magnitudes and orientation are somewhat suprising, because the independent strain indicators are only indirectly linked. Figure 9 shows the common physical relationship of chondrules and metal grains in chondrites. Petrofabric strain analysis is based on chondrules, and magnetic anisotropy is controlled by the shapes of metal grains, which are commonly situated between chondrules. Because chondrules may be more rigid (competent) than the maleable metal grains, the metal grains would presumably accomodate more strain than the chondrules. This may account for the fact that the magnetic anisotropy tends to be more strongly defined than the chondrule strain.

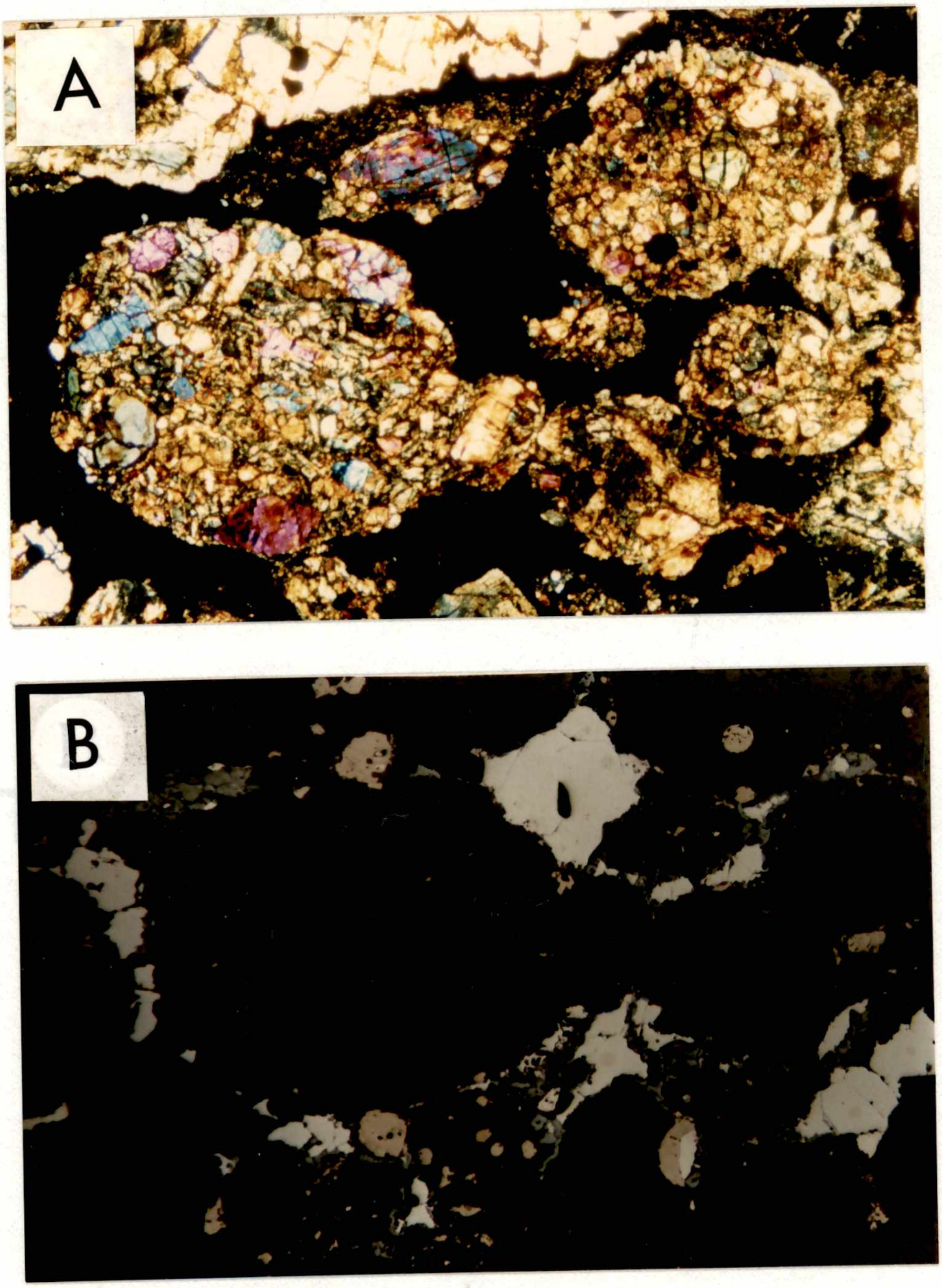

Figure 9. Photomicrographs displaying the physical relationship of chondrules and metal grains in ordinary chondrites. (A) This transmitted light photomicrograph shows oblong chondrules with a preferred orientation. (B) Metal grains are commonly found situated between or rimming chondrules as evidenced by the same photomicrograph taken in reflected light. The field of view in these photos is 3.0mm.

Petrologic and Physical Comparisons

Of the fifteen samples analyzed, there were two LL, five L, and nine H chondrites. These samples range in petrologic type from Type 3 to 5 and range in deformation from 3-17% shortening along the principal minimum axis c) (Table 2). These strain and magnetic susceptibility measurements document the low to moderate deformation experienced by ordinary chondrites of low petrologic type. The most highly strained samples are consistantly L-group chondrites. This greater degree of deformation may be an inherent property of L-group chondrites. The L-group parent bodies formational history may have been more dynamic than the H- or LL-groups parent bodies, or the impact event that liberated the L-group chondrites may have been greater or more dynamic than those events in which the others were affected.

It has previously been shown that development of these fabrics is independent of the thermal history of the meteorites (Dodd, 1965). The data presented here support this lack of correlation in that increasing strain is not accompanied by an increase in thermal metamorphism in the samples.

Quantification and correlation of these two different types of strain measurements suggest something about their deformational history. The pancake shaped spheroids of the most deformed strain and susceptibility ellipsoids are consistent with the hypothesis that deformation was caused by shortening along the principal .pa minimum axes. This type of deformation could be due to either static or dynamic processes.

IV. SHOCK EFFECTS IN CHONDRITES

Optical Deformation Features

In order to understand the cause of deformation in chondrites, optical criteria of shock modified from Dodd et al. (1979) have been established. The classification scheme of Dodd et al. (1979) could not be directly applied to the samples in this study. The range of shock deformation discovered in this study is not very broad; therefore, a more sensitive set of criteria are necessary for unambiguous delineation of shock facies. In addition the three shock facies defined for this study are based entirely on petrographic observations of olivine, because of its abundance and because of the unmeasurable amount of plagioclase in chondrites of low petrologic type. Because olivine is the most abundant mineral in chondrules, it is assumed that if chondrules are deformed, then the olivines are as well.

The optical criteria of shock used to define the three shock facies are as follows: I = fractured olivine and minor undulatory extinction; II = fractured olivine and extensive undulatory extinction; and III = fractured olivine, extensive undulatory extinction and presence of mosaicism. Each sample was assigned to one of the shock facies (Table 5). Figure 10 shows that deformational features in olivine grains attributed to shock (Dodd et al., 1979) correlate with chondrule deformation.

Noble Gas Contents as Shock Indicators

Dodd et al. (1979) noted a relationship between depletion of noble gases and shock intensities in L-group ordinary chondrites. They

Table 5. Shock facies modified from Dodd et al., 1979

Mezo-Madaras (H)	II	Kesen	I
Mezo-Madaras (S)	II	Grady	I
McKinney	III	Ankober	I
Barratta	III	Clovis	I
Farmington	III	Faucett	I
Broken Bow	II	Hammond Downs	I
Parnallee	II	Adrian	I
Menow	II	Kelly	I

reported a depletion in the volumetric abundances of 4He and 40Ar, corresponding with the first appearance of shock-induced melt pockets. This elemental depletion is gradational and correlates with their increasing shock facies a-f (Dodd et al., 1979).

Abundances of 4He and 40Ar were available for twelve of the samples from this study (Shultz and Kruse, 1978). Figure 11 shows that samples of higher shock facies are consistently depleted in noble gases. The linear regression calculated for the noble gas data in this study corresponds closely to that in the work of Dodd et al. (1979). The most probable cause for variation is the difference in number and types of samples. This study used 12 samples, as opposed to 40 used by Dodd et al. (1979).

The 4He-40Ar plot used by Dodd et al. (1979) is also restricted to L-group chondrites, whereas this study used H-, L- and LL-group chondrites.

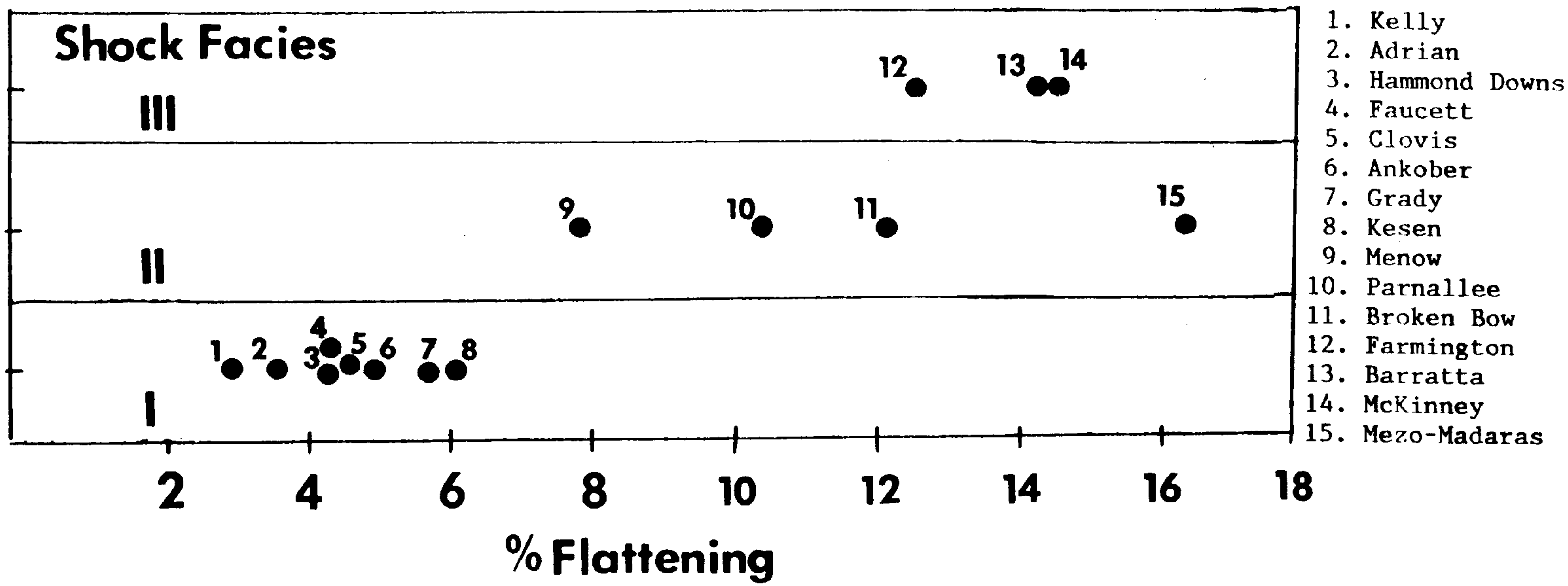

Figure 10. Optically defined shock facies vs. percent flattening plot. The percent flattening used for Mezo-Madaras is an average of the two samples measured in the straain analysis.

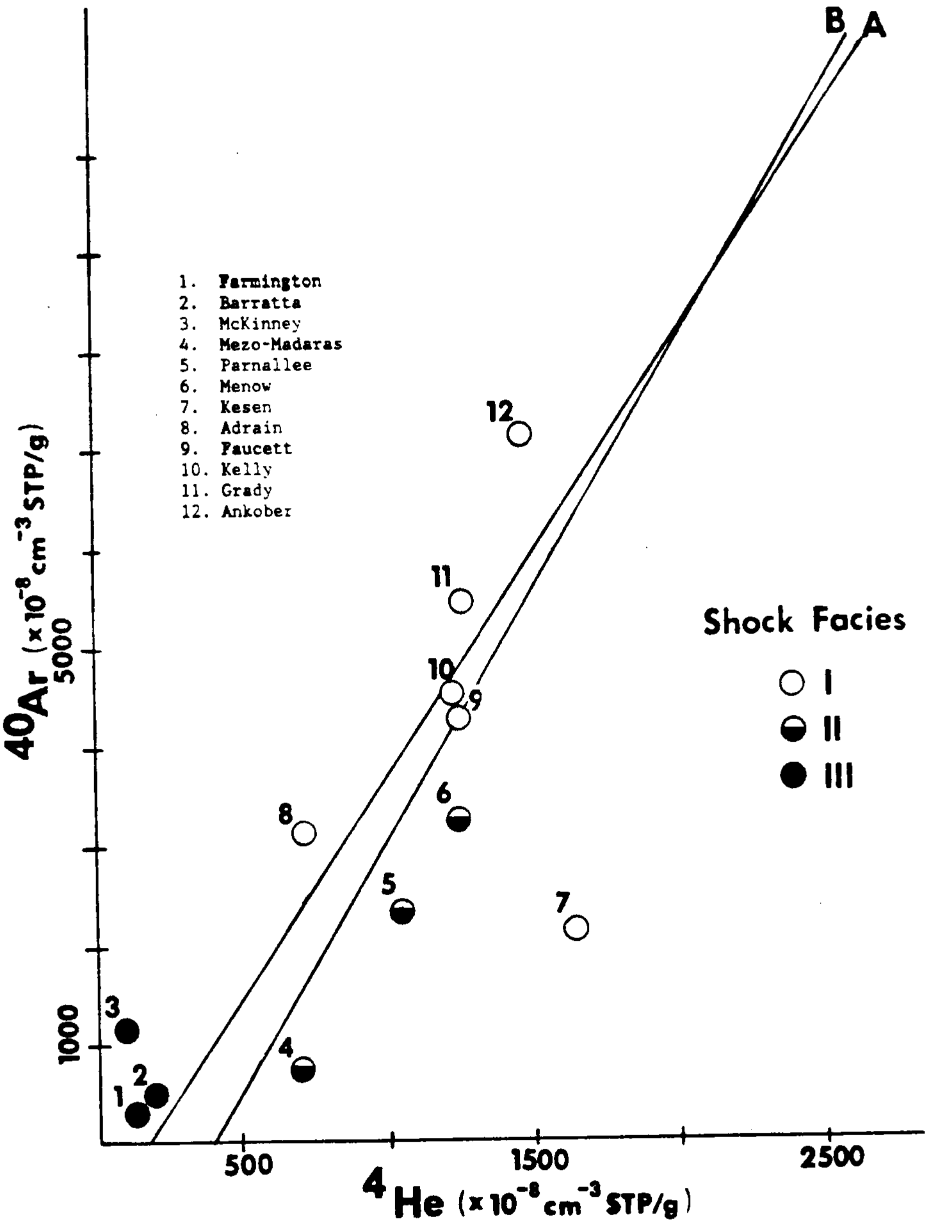

Figure 11. He vs. Ar plot showing relationship between noble gas depletion and increasing deformation intensity. Line A represents the linear regression through the shock facies data from this study. Line B represents the linear regression through the data of Dodd et al. (1979).

Transmission Electron Microscopy

Analysis of microscopic deformation provides further insight into the mechanism of chondrule deformation. Transmission Electron Microscopy (TEM) analyses of a severely strained and an essentially undeformed sample were performed to observe dislocation substructures in olivine grains within chondrules. Orientation, Burger's vectors, density, and geometrical relation of the dislocations were determined. Because dislocation glide systems and densities are dependent upon pressure, temperature, deviatoric stress, and strain rate (Gueguen, 1977), dislocation measurements in chondritic olivine samples should improve our knowledge of these parameters and allow a more constrained interpretation of the mechanism which deformed the chondrules.

Review of Dislocations

Generation and propagation of dislocations in olivine play a major role in its plastic deformation (Green and Radcliffe, 1972). Dislocations are described in terms of translation vectors which represent the displacement of atoms from their regular positions in the crystallographic lattice planes (Hull, 1975). These translation vectors are called Burgers vectors [b]. Identification of Burgers vectors allows complete definition of the type and orientation of dislocations imaged. When dislocations are imaged, they are said to be in contrast or are visible. Burgers vectors for individual dislocations are determined using the well documented invisibility criterion: for $g*b=0$, there is no contrast and dislocations in that orientation are invisible (g is defined as the reciprocal lattice plane vector as determined from the diffraction pattern imaged in reciprocal space). Thus, from the orientation of dislocations with respect to the Burgers vectors, the type of dislocation visible can be determined. A complete description of Burgers vector analysis methods may be found in Hirsch (1965) and Boland (1977).

When Burgers vectors are parallel to a dislocation line, the dislocations are of the "screw" type. When the Burgers vectors are perpendicular to the dislocation line, the dislocations are of the "edge" type. In the most general case, a dislocation line lies at an arbitrary angle to its Burgers vector and the dislocation line has a "mixed" srew and edge character (Hull, 1975). The g*b=0 criterion for invisibility has been experimentally tested, proving its validity for determining Burgers vectors for screw and edge dislocations (Radcliffe et al., 1970).

Kohlstedt and Goetz (1974) established that deformational strain in olivine crystals is associated with dislocation motions. The two basic types of dislocation movement are glide and climb. Movement of dislocations at low temperatures, where diffusion is difficult, is limited almost entirely to glide along closest packed atomic planes. Climbing processes require mass transport by diffusion and therefore a higher thermal activation energy is necessary. Higher temperature conditions thus allow dislocations to climb out of their slip planes (Hull, 1975). Structures indicative of climb, and thus higher thermal energy, are curved dislocations, loops and "helical-like" dislocations.

Previous Work

It is important to identify dominant mechanisms of deformation though, because this determines how measurable strains are related to deviatoric stress, temperature, and strain rate. Olivine is one of the most common minerals in ordinary chondrites. Substructures produced in olivine grains by deformation are easily observable compared to the complex nature of those in pyroxenes.

Carter et al. (1968) optically described the plastic deformation of olivines in naturally deformed ordinary chondrites. Their results indicated that slip systems were crystallographically controlled, and they varied with temperature and strain rate. Ashworth (1975) compared experimentally deformed terrestrial olivine substructures with naturally deformed meteoritic olivine. Parameters of strain rate, temperature, and dislocation densities varied with substructure type and orientation in meteoritic olivine in the same manner as the terrestrial olivine substructures. This study confirmed two ideas previously established by Blacic and Christie, (1973) Green and Radcliffe (1972) and Phakey et al., (1972c): 1) slip parallel to [100] dominates at relatively higher temperatures, lower stresses, and slower strain rates, whereas slip parallel to [001] dominates at relatively lower temperatures, higher stresses, and faster strain rates; 2) principal Burgers vectors in olivine are [100], [001], and [010]. The collective results of the terrestrial studies indicated that the transition from [100] to [001] occurs at approximately 1000°C for a strain rate of 1x10-5, s-1 but the boundary is tenuous. These TEM studies also report a dominance of screw dislocations of both [100] and

[001] Burgers vectors in the dislocations in experiments at all temperatures.

Sears et al. (1984) performed an extensive study of artificially shocked chondrites over a range of pressures. Pressures of 70 to 270 kbar generated long, straight [001] screw dislocations with a few edge segments. Increasing shock pressure was paralleled by an increase in density of the same types of dislocations, with a maximum density of $3x10^{+9}$ cm^{-2}. The relationship between stress and dislocation density has been extensively documented in terrestrial olivine analyses. Dislocation densities of 10^{+9} to 10^{+10} (long, straight [001] screws) were observed in experimentally deformed olivine at 800°C, 10^{-5} sec^{-1}, while densities of 10^{+6}-10^{+7} (b=[100]) were observed at 1000° to 1100°C, 10^{-7} to 10^{-11} sec^{-1} (Gueguen, 1977). This correlation supports the hypothesis that overall dislocation density decreases with decreasing stress.

Ashworth et al. (1985) studied the natural, relatively severe effects of shock in ordinary chondrites. They compared their results to experimentally shocked chondrites (Sears et al. 1984) and favorably tested applicability of experimental shock data in interpreting natural phenomena. They concluded that deformation and recovery effects of olivine justify the use of this phase as a good indicator of shock.

Experimental Techniques

All transmission electron microscopy measurements and interpretations were made under the supervision of G. Nord at the United States Geologic Survey in Reston, Virginia.

Thin section preparation methods of Wandless et al. (1986) were employed. Doubly polished, demountable thin sections (25-30 microns) were examined in detail under the petrographic microscope to identify phases and to select crystals for analysis. The selected areas were detached from the sample and fixed to a copper washer-type mount (3.0 mm diameter). These samples were then ion-beam thinned to 50-100 Å with an argon plasma discharge until electron transparency was attained. Microphotographic comparison was made before and after thinning to facilitate identification of selected analysis areas in the electron microscope. The specimens were carbon-coated and mounted in a high-voltage (200 Kv) JOEL transmission electron microscope. A double-tilt stage was used so that minerals and their orientations could be identified using electron diffraction patterns. Two-beam diffraction conditions were used to identify intracrystalline deformation structures. Burgers vector analyses were performed to more completely characterize substructure type and orientation. The study was restricted to olivine in porphyritic olivine-pyroxene chondrules, because they are by far the most abundant type of chondrules found in ordinary chondrites. Barred olivine chondrules were avoided because their formation under a higher temperature regime may have induced substructures that were unrelated to the deformation in question.

Observations

McKINNEY: The strain analysis performed on McKinney shows it to be one of the most deformed samples (Fig. 1d-f). Optically, the olivine grains in this chondrite show multiple fractures, extensive undulatory extinction, and mosaicsm, indicating a " moderately-shocked" condition as defined by Carter et al. (1968).

Deformation substructures are very common in all samples observed. The dislocations predominantly have long, curved segments of relatively complex character that are aligned parallel to a [010] Burgers vector (Fig. 12a). The [010] lines are in contrast for g values of 020 and 010 and out of contrast for 102. Thus the slip regime observed for McKinney is {h01}[010]. In McKinney, [010] screws are overwhelmingly the predominant type of dislocations, although some edge and mixed components are present. When the g vector is placed in the 1 position, dislocations with Burgers vector [001] are inferred. Although orientation of the sample prohibited contrast analysis for g=001, dislocations where g=102 were in contrast, allowing inference of b=[001] by the invisibility criterion g*b=0. The dislocations viewed in this orientation are parallel to [001], thus characterizing screw-type dislocations. Dislocation densities of 5x10+9 cm-2 are distributed homogeneously throughout the grains. The density is so high that some areas are completely black with dislocations; therefore, the density could not be ascertained.

The complex character of dislocations previously mentioned includes presence of curved lines, loops, jogs, and curly or "helical-like" dislocations imprinted on subgrains (Fig. 12b). The occurrence of curved dislocations and loops is indicative of olivine that has experienced high enough temperatures for the diffusive process of dislocation climb to have been important. The minor presence of jogs

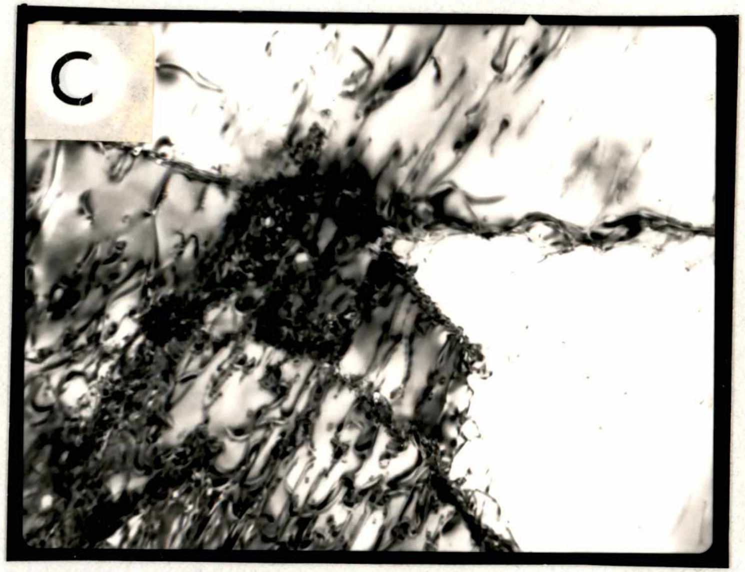

Figure 12. Transmission electron micrographs of McKinney. (A) displaying complex character of dislocations; (B) loops and jogs indicating moderate recovery of the sample; (C) subgrains imprinted with dislocations of complex character. The scale for each photomicrograph is 25mm = 1 micron.

and "helical-like" dislocations also indicates motion out of the slip plane.

Misorientation along the subgrain boundaries is small, thus inhibiting identification by optical microscopy. The complex substructures displayed in Figure 12b are also observed overprinting the subgrains.

ADRIAN: The strain analysis performed on Adrian shows it to be one of the least deformed ordinary chondrites in this study (Fig. 2d-f). Optically, the olivine grains are fairly clean in terms of fractures and show an uneven distribution of undulatory extinction. These petrologic features classify Adrian as "lightly-shocked" according to Carter et al. (1968).

Deformation substructures are fairly common in all samples observed. The dislocations predominantly have long straight segments of simple character that are aligned parallel to a [001] Burgers vector (Fig. 13a). In two-beam experiments, the dislocations were in contrast for $\underline{g}$= 001, 002 and 011 and out of contrast for $\underline{g}$= 010, thus defining the slip regime for Adrian to be {hk0}[001]. [001] screws are overwhelmingly the most abundant type of dislocation, although a few edge and mixed components are observed. When dislocations with $\underline{g}$=010 and 011 were in contrast and out of contrast for $\underline{g}$= 001, a second Burgers vector [010] was defined. The character of dislocations was the same as for b=[001], except the density was much lower and edge segments were dominant. When contrast conditions of g= 011 were applied to observe dislocations, structures seen in both [001] and [010] orientations were visible, as well as some new dislocations that were

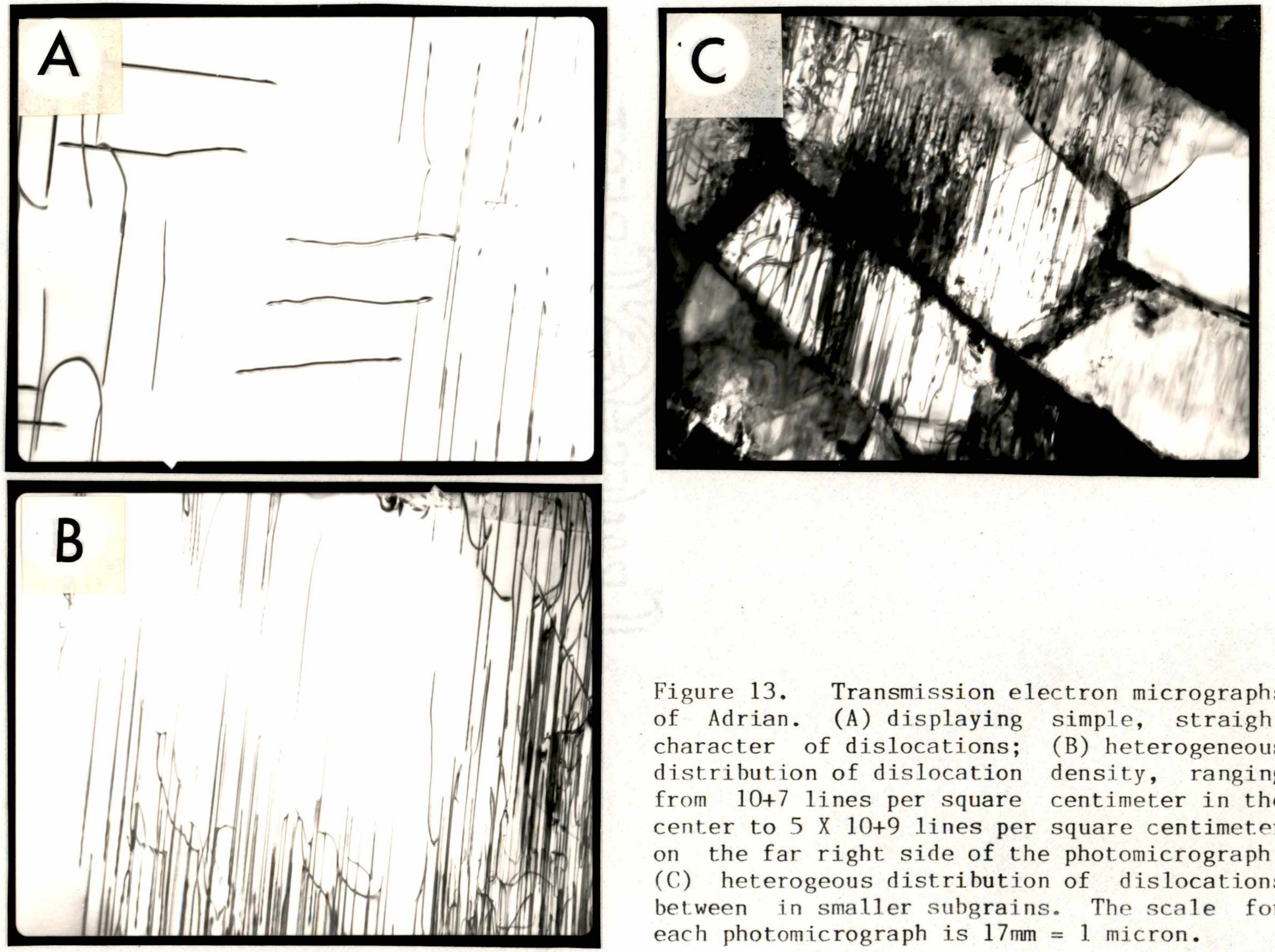

Figure 13. Transmission electron micrographs of Adrian. (A) displaying simple, straight character of dislocations; (B) heterogeneous distribution of dislocation density, ranging from 10+7 lines per square centimeter in the center to 5 X 10+9 lines per square centimeter on the far right side of the photomicrograph; (C) heterogeous distribution of dislocations between in smaller subgrains. The scale for each photomicrograph is 17mm = 1 micron.

previously invisible for [001] and [010]. These new dislocations possibly define a unique Burgers vector [011], although it has been suggested that [011] is simply a combination of [001] and [010]. A total then of three Burgers vectors are observed in Adrian; however, only two are probably unique.

Subgrains overprinted by long, straight dislocations were also observed in Adrian. No noticable gradation in terms of degree of subgrain development was noticed when comparing Adrian and McKinney. The character of dislocations observed in McKinney is very complex and indicative of partial recovery. The straight, simple character of dislocations in Adrian have apparently undergone a lesser degree of recovery. The deformational event, imprinting the straight dislocations then, must have been under much cooler conditions than the deformational event that affected McKinney. Dislocation glide dominates in most samples, except in a few cases where loops and curly dislocations appear to be trying to climb out of the lattice plane.

Dislocation densities are inhomogeneous throughout all of the samples of Adrian. Densities that range from 10+7-10+9 over only 3 microns indicate their heterogeneous distribution (Fig. 13b). The comparatively low density and the simple, straight character of dislocations in Adrian allowed easier measurement of density than in McKinney.

Heterogeneous distribution of dislocations in subgrains seems to show a higher density in smaller subgrains and a lower cluster in the larger subgrains (Fig. 13c). This type of observation was explained in analogous material in shocked lunar samples, as the heterogeneous effects of shock (Lally et al., 1976). This explanation is dependent on attenuation of shock waves occurring primarily at crystalline discontinuities. Thus, in the lunar dunite sample examined, shock primarily occured at grain boundaries. The larger clasts in the lunar study were much more transparent to the shock, allowing many of the shock waves to pass through without .pa noticable affect. Consequently, fewer dislocations accumulated in the larger grains than in the smaller ones.

V. ORIGIN OF STRAIN IN CHONDRITES

Three hypotheses have been proposed to explain foliations observed in ordinary chondrites: sedimentary accretion, deformation due to overburden pressure, and shock deformation. It is unlikely that the rock fabrics measured in this study are primary sedimentary accretional features as proposed by Dodd (1965). It is difficult to envision a nebular process that would promote the differential segregation of chondrules as a function of the degree of flattening. Instead, they almost surely developed by deformation in situ during or after accretion.

Cain et al. (1986) proposed static deformation to have occured as a result of compaction due to accretionary overburden. In light of the new observations and correlations in this study, it will be shown that reliance on the deformation model proposed by Cain et al. (1986) is not necessary for the samples examined. The idea of Ashworth et al. (1975b, 1977) that most meteorites have suffered shock to some degree, during and after disaggregation of their parent body, is the most commonly accepted mechanism for chondrite deformation.

Evidence For Shock Deformation

TEM

Despite the fact that the mechanics of shock as it effects chondrites are not completely understood, many characteristics of shock behavior have been described. Shock deformation occurs generally at low temperatures, very high strain rates (10+7-10+9 sec-1), and stresses in the megabar range (Christie et al., 1976). Out of the 53 L-group chondrites studied by Dodd et al. (1979), only four were found to be essentially devoid of shock effects. In the TEM analyses of McKinney and Adrian, shock effects seem to be responsible for the deformation of olivine in chondrules.

The remarkably different character of dislocations observed in McKinney versus Adrian allows inference of their thermal state during deformation. Both samples contain subgrains overprinted by dislocations of varying character. The subgrains are interpreted to have formed during primary igneous crystallization of olivine grains (G. Nord, per comm., 1986). Subgrains with rectangular and sharp corners are indicative of formation during crystallization. Apparently the lattice planes were strained during crystallization and dislocations subsequently recovered into subgrain boundaries while the olivine was still hot. The dislocations overprinting subgrains in McKinney are much more complex than those in Adrian, indicating that the deformational event that imposed the substructures, occurred while McKinney was still relatively hot.

Because the dislocations overprinting the subgrains are the ones that have been deformationally induced, they are the substructures of interest to this study. [001] screw dislocations form in a relatively low-temperature, high-strain-rate, and high-stress environment in experimentally and naturally deformed olivines. The transition boundary between [001] and [100] slip systems varies as a function of stress and is poorly defined. [001] screw and edge components are the predominant types of dislocations found in both

McKinney and Adrian. The presence of these types of dislocations allows the inference to be made however, on the mechanism of deformation i.e. shock deformation. When the qualitative parameters related to deformation by shock (low-temperature/high-strain-rates) are compared to dislocation densities in the samples, the inference of deformation by shock processes is suggested. Dislocation densities on the order of 10+9 cm-2 and greater in some areas can only have formed at very high strain rates and under an extreme stress. Shock strain rates of 10+7 to 10+9 sec-1 (Christie et al., 1976) correspond most closely to dislocation densities of the magnitude found in this study (G. Nord, per. comm., 1986). Therefore, despite the ambiguity in constraining deformational conditions by use of Burgers vectors, the density of McKinney and Adrian substructures can be used as an indicator of a shock deformational history.

The heterogeneous distribution of dislocation densities in Adrian further suggests substructure generation by shock. Unequilibrated chondrites are composed of large, solid chondrules and large grains of silicates, sulfides, and metals, enclosed in a porous, fine-grained matrix. In such an inhomogeneous medium, shock waves are reflected and refracted at grain boundaries, creating areas of energy concentration. Shock can thus result in heterogeneous mechanical deformation of a chondrite and may be responsible for the observed heterogeneity in dislocation densities over short distances (Scott and Rajan, 1981). This variation in intensity, due to shock deformation, is exemplified in Adrian, where dislocation densities vary from 10+7-10+9 cm-2 over a distance of less than 3 microns.

The gradation of strain, quantified by the chondrule strain and magnetic anisotropy measurements is consistent with the range in degree of dislocation densities observed using TEM. Adrian shows an overall lower density of dislocations, while McKinney has a homogeneously high dislocation density. Adrian has been shown to have essentially the least strained chondrules and most poorly defined magnetic anisotropy. Conversely, McKinney is comparatively highly deformed, as evidenced by its well defined chondrule and magnetic foliations.

Micro-Deformation Mechanisms

The dominant mechanism of olivine deformation, based on these TEM results, appears to be low-temperature plasticity. Low-temperature plasticity is a plastic deformation involving the gliding motion of dislocations (Ashby and Verrall, 1977). This type of plasticity is observed at low temperatures and high stress, with slip systems varying from [001] to [010] to [100] with increasing temperature. Power-law creep is a non-linear flow involving both the climb and glide motion of dislocations (Ashby and Verrall, 1977). The two samples analyzed fall within the low-temperature plasticity deformational field; however, effects of dislocation climb are evident. Presence of curved dislocations, dislocation loops, and "helical-like" dislocations demand higher temperatures for diffusion of dislocations. There is a limit on maximum temperatures experienced by McKinney (L4) and Adrian (H4) though, ranging from 600°C to 700°C (Dodd, 1981). This limitation essentially constrains the mechanism of deformation to low-temperature plasticity; however, power-law creep was probably a minor component in the deformation as well.

The TEM analyses suggest, therefore, that the deformation of chondrule olivines by dominantly low-temperature plasticity was caused by a progression of shock intensities affecting different samples as evidenced by dislocation densities.

Noble Gases

Figure 10 displays the gradation in deformation based on shock facies (defined by optical shock criteria similar to Dodd et al., 1979). This gradation correlates to the gradation of percent flattening quantified in the strain analysis for each sample. Because percent shortening is the numerical description of the degree of foliation development observed in the samples, this gradation in foliation is therefore caused by deformation.

The concentrations of 4He and 40Ar for twelve samples were shown to correlate with shock facies in Figure 11. Because the depletion of noble gases is directly proportional to the gradation in shock facies, it can be assumed that the noble gas depletion is also related to increasing strain.

Concentrations of 4He and 40Ar are sensitive indicators of shock intensity (Dodd et al., 1979). Increasing shock intensity, as defined by optical shock criteria, is related to the depletion of these light noble gases. Because increasing strain is accompanied by 4He-40Ar depletion, it is concluded that the strain observed is shock-induced. The TEM data support this dynamic mechanism gf deformation for chondrites as well.

Pressure Calibration

Assuming shock has been established as the mechansim of deformation for these samples, peak pressures can be calibrated using optical shock criteria in comparison with experimentally shocked samples. An ordinary chondrite [EET 83213] has been experimentally shocked at impact velocities ranging from 1.184 to 1.775 km/sec in an attempt to calibrate pressures experienced by samples in this study (F. Horz, per. comm., 1986). Peak pressures were subsequently determined, ranging as a function of projectile material density and target container material from 49 to 199 GPa (Table 6). The mineralogy and type of chondrules present in the unshocked chondrite are very similar to the essentially undeformed samples in this study. Using the same optical shock criteria, these experimentally shocked samples were assigned to their appropriate shock facies (Table 6).

Sample 1352 experienced the highest peak pressure (199 GPa) and was the only sample that displayed extensive mosaicism of grains. A fourth shock facies was therfore established for the experimental samples because of the unique nature of this sample. Two thin sections were made from each sample: a plan view and a cross-section. It would have been interesting to attempt to measure any foliation that the shock deformation created. Unfortunately the cross-sectional views were too narrow to enclose whole chondrules, thus prohibiting optical observation of increasing chondrule deformation with increasing peak pressure.

By considering optical properties and their correlation with peak pressures from Sears et al. (1984), Dodd and Jarosewich (1979) and the

Table 6. Peak pressures for experimentally shocked chondrite [ETT 83213]

Sample #	Projectile Material	Target Container Material	Impact-Velocity (Km/s)	Peak Pressure (GPa)	Shock Facies
1347	Al	SS	1.184	147	III
1348	Lexan	Al	1.193	49	I
1349	Al	SS	1.438	124	II
1350	Al	SS	1.210	151	III
1351	Al	SS	1.385	177	III
1352	Al	SS	1.527	199	IV
1353	Lexan	Al	1.775	76	II

Al = Aluminum 2024
SS = Stainless Steel 304

experiment above, extrapolations can be made to this study. Considering intracrystalline properties observed in McKinney and Adrian, and optical properties of the other samples, the peak pressures experienced can be constrained from <70 to 177 GPa. Samples experiencing peak pressures of greater than 199 GPa develop mosaicism of olivine grains as well as b=[100] dislocations (Sears et al., 1984). Samples experiencing peak pressures of less than 70 GPa generally have little (if any) undulatory extinction, and that only in a few grains.

One question remains when considering shock as the deformation mechanism necessary to create foliations in ordinary chondrites: Why are foliations not obvious in some of the most severly shocked meteorites? A possible answer is that severe shock deformation is accompanied by brecciation and broken chondrules. The combination of these constituents might obscure any shock-induced foliation. Many of the samples in this study have planar fabrics that are not immediately evident. Without the strain analysis procedures utilized in this study, the deformation now quantified may have gone undetected.

The two independent, correlatable types of strain measured in each sample have therefore provided evidence for the physical processing of ordinary chondrites. The chondrule- and metal-defined foliations measured are apparently shock-induced.

REFERENCES

REFERENCES

Ashby, M.F., and Verall, R.A., 1977. Micromechanisms of flow and fracture, and their relevance to the rheology of the Upper Mantel, Philos. Trans. R. Soc. London, Ser.A 288, 59-95.

Ashworth, J.R., 1985. Transmission electron micrgscopy of L-group chondrites, 1. Natural shock effects, Earth and Planetary Scienc Letters, 73, 17-32.

Ashworth, J.R., and Barber, D.J., 1975b. Electron petrography of shock-deformed olivine in stony meteorites, Earth and Planetary Science Letters, 27, 43-50.

Ashworth, J.R., and Barber, D.J., 1977. Electron microscopy of some stony meteorites, Phil. Trans. R. Soc. London. A 286, 493-506.

Binns, R.A., 1967d. Structure and evolution of noncarbonaceous chondrites. Earth and Planetary Science Letters, 2, 23-28.

Blacic, J.D., and Christie, J.M., 1973. Dislocation substructure of experimentally deformed olivine, Contributions to Mineralogy and Petrology, 42, 141-146.

Boland, J.N. and Buiskool Toxopeus, J.M.A., 1977. Dislocation deformation mechanisms in peridotite xenoliths in kimberlites. Contrib. Mineral. Petrol., 60, 17-30.

Borradaile, G.J., 1984. Strain analysis of passive elliptical markers: success of de-straining methods, Journal of Structural Geology, vol. 6, No. 4, 433-437.

Brecher,A., 1977. Interrelationships between magnetization directions, magnetic fabric and oriented petrographic features in lunar rocks, Proc. Lunar Sci. Conf. 8th, 703-723.

Bunch, T.E. and Stoffler, D., 1974. The Kelly chondrite: A parent body surface metabreccia. Contrib. Mineral. Petrolog., 44, 157-171.

Cain, P.M., McSween, H.Y., and Woodward, N.B., 1986. Structural deformation of the Leoville chondrite, Earth and Planetary Science Letters, 77, 165-175.

Carter, N.L., Raleigh, C.B., and DeCarli, P.S., 1968. Deformation of olivine in stony meteorites. Journal of Geophysical Research, vol. 73, no. 16, 5439-5461.

Christie, J.M. and Ardell, A.J., 1976. Deformation structures in minerals. In: Electron Microscopy in Mineralogy, H.R. Wenk, editor. Springer-Verlag.

Cloos, E., 1947. Oolite deformation in the South Mountain fold, Maryland, Geol. Soc. Am. Bull., 58, 843-918.

Dodd, R.T., 1981. Meteorites: a Petrologic-Chemical Synthesis, Cambridge University Press.

Dodd, R.T., Van Schmus, W.R., and Koffman, D.M. 1967a. A survey of the unequilibrated ordinary chondrites, Geochim. Cosmochim. Acta 31, 921.

Dodd, R.T. and Van Schmus, W.R. 1965a. Significance of the unequilibrated ordinary chondrites, J. Geophy. Res. 70, 3801.

Dodd, R.T., 1965. Preferred orientation of chondrules in chondrites, Icarus, 4, 308-316.

Dodd, R.T. and Jarosewich, E., 1979. Incipient melting in and shock classification of L-group chondrites. Earth and Planetary Science Letters, 44, 335-340.

Dunnet, D., 1969. A technique of finite strain analysis using elliptical markers, Tectonophysics, 7, 117-136.

Dunnet, D., and Siddans, A.W.B., 1971. Non-random sedimentary fabrics and their modification by strain, Tectonophysics, 12, 307-325.

Fredriksson, K., Nelen, J., and Fredriksson, B.J. 1968a. In: Ahrens, L.H., (Ed.): Origin and Distribution of the Elements, p.457. New York-London: Pergamon.

Fry, N., 1979. Random point distributions and strain measurements in rocks, Tectonophysics, 60, 89-115.

Gooding, J.L. and Keil, K., 1980. Relative abundances of chondrule primary textural types in ordinary and their bearing on conditions of chondrule formation. Meteorites, vol. 16, no. 1, 17-43.

Green, H.W. II, and Radcliffe, S.V., 1972c. Dislocation mechanisms in olivine and flow in the upper mantel, Earth and Planetary Science Letters, 15, 239-247.

Gueguen, Y., 1977. Dislocations in mantle peridotite nodules. Tectonophysics, 39, 1-3, 231-254.

Hamano, Y., and Yomogida, K., 1982. Magnetic anisotropy and porosity of Antarctic chondrites, Proc. 7th Symposium on Antarctic Meteorites, 281-290.

Hirsch, P.B., Howie, A., Nicholson, R.B., Pashley, D.W. and Whelan, M.J., 1965. Electron Microscopy in Thin Crystals. London: Butterworth.

Hull, D., 1975. Introduction of Dislocations, Second edition. Pergamon Press.

Huss, G.R., Keil, K., and Taylor, J.G., 1981. The matrices of unequilibrated ordinary chondrites: implications for origin and history of chondrites. Geochim. Cosmochim. Acta, vol. 45, pp33-51.

Keil, K. and Fredriksson, K. 1964a. Coexisting olivines and rhombic pyroxenes of chondrites, J. Geophy. Res., 69, 3487.

Keil, K., 1982. Composition and origin of chondritic breccias. From: "Workshop on Lunar Breccias and Soils and their Meteoritic Analogs," LPI Tech. Rep. 82-02, 65-107.

Kligfield, R., 1982. Programs for strain analysis, editor, (Boulder version).

Kligfield, R., Lowrie, W., and Pfiffner, A.O., 1982. Magnetic properties of deformed oolitic limestones from the Swiss Alps: the correlation of magnetic anisotropy and strain. Eclogae Geol. Helv., vol. 751, pp. 127-157.

Kohlstedt, D.L. and Goetze, C., 1974. Low stress, high-temperature creep in olivine single crystals. Journal of Geophysical Res., 79, 2045-2051.

Lally, J.S., Christie, J.M., Nord, Jr., G.L., and Heuer, A.H., 1976. Deformation, recovery and recrystallization of lunar dunite 72417. Proc. Lunar Sci. Conf. 7th, 1845-1863.

Lisle, R.J., 1977. Clastic grain shape and orientation in relation to cleavage from the Aberystwyth Grits, Wales, Geol. in Mijnb., 56, 140-144.

Lisle, R.J., 198??. Geological Strain Analysis: A Manual for the Rf/Phi Method, Pergamon Press.

Martin, P.M., Mills, A.A., and Walker, E., 1975. Preferred orientation in four CV3 chondritic meteorites, Nature, 257, 37-38.

Martin, P.M. and Mills, A.A., 1976. Size and shape of chondrules in the Bjurbole and Chainpur meteorites, Earth and Planetary Science Letters, 33, 239-248.

Martin, P.M., and Mills, A.A., 1978. Size and Shape of near-spherical Allegan chondrules, Earth and Planetary Science Letters, 38, 385-390.

Martin, P.M. and Mills, A.A., 1980. Preferred orientations in meteorites, Earth and Planetary Science Letters, 51, 18-25.

Mason, B. 1963a. Olivine composition in chonmdrtes, Geochim. Cosmochim. Acta 27, 1011.

Mason, B. 1967a. Olivine composition in chondrites - a supplement, Geochim. Cosmochim. Acta 31, 1100.

Mason, B. 1973a. Hammond Downs, a new chondrite from the Tenham area, Queensland, Australia, Meteoritics 8, 1.

Means, W.D., 1976. Stress and Strain, Springer-Verlag New York Inc.

Peach, C.J., and Lisle, R.J., 1979. A fortran IV program for the analysis of tectonic strain using deformed elliptical markers, Computers and Geosciences, vol. 5, 325-334.

Phakey, P., Dollinger, G. and Christie, J.M., 1972. Transmission electron microscopy of experimentally deformed olivine. In: H.C. Heard, I.Y. Borg, N.L. Carter and C.B. Raleigh (editors). Flow and Fracture of Rocks. Geophys. Monogr., am. Geophy. Union, 16, 139-156.

Radcliffe, S.V., Heuer, A.H., Fisher, R.M., Christie, J.M. and Griggs, D.T., 1970. High voltage (800Kv) electron petrography of type B rock from Apollo 11. Proc. Apollo 11 Lunar Sci. Conf., 1, 731-748.

Ramsey, J.G., 1967. Folding and Fracturing of Rocks, McGraw-Hill Book Co., New York.

Rubin, A.E., Rehfeldt, A., Peterson, E., Keil, K. and Jarosewich, E., 1983. Fragmental breccias and the collisional evolution of ordinary chondrite parnet bodies. Meteorites, vol. 18, no. 3, 179-196.

Scott, E.R.D. and Rajan, R.S., 1981. Metallic minerals, thermal histories and parent bodies of some xenolithic, ordinary chondrite meteorites. Geochim. Cosmochim. Acta, 45, 53-67.

Scott, E.R.D., Taylor, G.J., Rubin, A.E., Okada, A. and Keil, K. 1981. Graphite-magnetite aggregates in ordinary chondritic meteorites. Nature vol. 291, 544-546.

Sears, D.W., Ashworth, J.R., Broadbent, C.P., and Bevan, A.W.R., 1984. Studies of an artificially shock-loaded H-group chondrite, Geochim. Cosmochim. Acta, 48, 343-360.

Shultz, L. and Kruse, H. 1978. Light noble gases in stony meteorites - a compilation. Nucl. Track Detection 2, pp65-103.

Siddans, A.W.B., 1980. Analysis of three-dimensional, homogeneous, finite strain using ellipsoidal objects, Tectonophysics, 64, 1-16.

Stacey, F.D., Lovering, J.F., and Parry, L.G., 1961. Thermomagnetic properties, natural magnetic moments, and magnetic anisoropies of some chondritic meteorites, Journal of Geophysical Research, vol. 66, No. 5, 1523-1534.

Sugiura, N., and Strangway, D.W., 1983. Magnetic anisotropy and porosity of chondrites, Geophysical Research Letters, vol. 10, No. 1, 83-86.

Van Schmus, W.R., 1967. Polymict structure of the Mezo-Madaras chondrite. Geochim. Cosmochim. Acta 31, 2027-2042.

Van Schmus, W.R. and Wood, J.A., 1967. A chemical-petrologic classification for the chondritic meteorites. Geochim. Cosmochim. Acta, 31, 737-765.

Wandless, M.-V., and Nord, G.L.,Jr., 1986. Sample preparation techniques for transmission electron microscopy of geologic materials, U.S.G.S., Open-File Report 86-255, 1-20.

Weaving, B., 1962. Magnetic anisotropy in chondritic meteorites, Geochim. Cosmschim. Acta, 26, 451-455.

APPENDICES

APPENDIX I

APPENDIX I

Methods of Strain Analysis

Many methods for analyzing finite strain in rocks have been developed (Cloos, 1947; Dunnet, 1969; Fry, 1979; Siddans, 1980; Lisle, 1977; Ramsey, 1967; Borradaile, 1984). An array of strain analysis software based on these techniques has been edited by Kligfield et al. (1982). The Tektronix hardware specifically suited for these programs consists of the following: 4052 Microcomputer with 64K memory and interactive graphics; 4956 (20x20 inch) Graphics tablet (digitizer); 4611 Hard copy unit for producing copies of whatever is on the screen of the 4052 instantly. The software used in this study, written in Tektronix basic, includes a set of four programs equipped to analyze two- and three-dimensional finite strain. This array of strain analysis programs from the Kligfield et al. (1982) package relies on initial assumptions of naturally deformed, homogeneous, and strained passive (no ductility contrast) markers.

The initial step of the strain analysis was utilization of the ELLIPSE-TRACING program on each face. This program generates a data set for each face of the sample from which the other programs base their interpretations. Acquisition of cubic samples is necessary in determining the three-dimensional strain imposed on each meteorite. Three mutually perpendicular thin sections from each cube were placed directly in an enlarger to make photographs for measurements (Dunnet, 1969). These photographs were arbitrarily oriented in a right-handed "up" orthogonal reference system. Although the pre-strained shape of chondrules is unknown, they can still be used as strain markers (Dunnet, 1969; Lisle, 1985). By digitizing the perimeters of chondrules, the ellipse-tracing program generates a best fit ellipse for each chondrule. From each ellipse, values of Rf, Ø and a correlation coefficient, showing the amount that the shape of the digitized perimeter deviates from a perfect ellipse with the same dimensions are calculated. This program is applied to three orthogonal photographs from each sample and the data are stored on a magnetic tape cartridge for input to the Rf/Ø and THETA programs. Optimal sample sizes for the Rf/Ø and THETA programs were investigated by Borradaile (1984). He found a marked improvement in sensitivity as sample sizes approached 50 markers but improvement beyond 75 markers became less pronounced. Between 20-90 chondrules were used on each photograph depending upon the size of sample available and degree of textural integration.

The Rf/Ø method of strain analysis is outlined by Ramsey (1967) and described in detail by Dunnet (1969) and Dunnet et al. (1971). Although this technique imposes no restrictions on the initial shape of the strain markers (Ri), it does assume that initial shapes were lacking in preferred orientation (Lisle, 1977). The Rf/Ø computer program provides two-dimensional strain analysis of individual sample faces, utilizing values of Rf (final deformed partical axial ratio) and Ø (angle from the Rf long axis to the maximum principal strain direction) generated by the ellipse tracing program (Fig. 14). The Rf data is shifted about its median value and centered around a vertical logarithmic Rf scale. The data are then shifted about their median

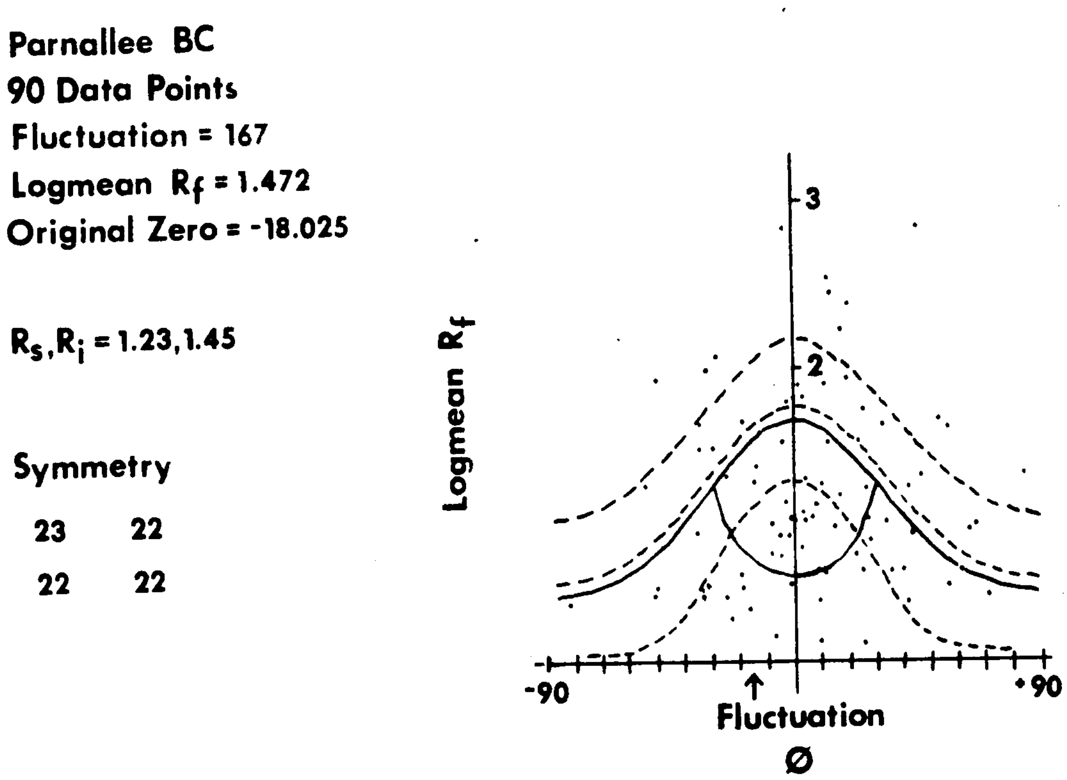

Figure 14. Rf/Ø example graph showing symmetry, fluctuation, original zero, Rs, Ri, logmean Rf and hyperbolic and Rf/Ø curves that best fit the data. The arrow beneath the fluctuation axis denotes the position of the original zero.

value along one of two horizontal scales, depending on the fluctuation of θ with respect to the vertical scale. The negative of the "original zero" parameter gives the value, in the original reference frame, of the median about which the data are shifted. This parameter thus is taken as the provisional direction of strain. The harmonic mean is taken from final axial ratios (Rf) of each chondrule to produce a mean final axial ratio for each face. The program allows the operator to progressively choose Rs (finite axial ratio of chondrules) and Ri values until a pair generates a hyperbolic curve that qualitatively best fits the data. The hyperbolic curve generated by Rs and Ri is defined by Rs occupying the minimum point of curvature and the length of the curve being a function of Ri. The log mean Rf value provided by the program may initially be used in determining Rs. The log mean Rf will nearly approximate Rs but will always take a slightly higher value than Rs becauses. The log mean Rf will nearly approximate Rs but will always take a slightly higher value than Rs because Rfmax is the product of Rs and Ri (Lisle, 1985). The symmetrical distribution of data points in four quadrants, defined by the vector mean θ and the Rs value, is also used as a guide in determining Rs and Ri. The program computes four symmetry values for each Rs value chosen, based on the number of data points in each quadrant. These quadrants should have equal points: A/B:C/D, where A=B=C=D. An asymmetrical distribution of data points, numerically describing a skew in the data, indicates lack of an initially random orientation of markers prior to deformation. These quadrants should have a skewed symmetry: A/B:C/D, where A=B,C=D or A=C,B=D. Also, a low concentration or lack of data points around the center Rf of the scatter indicates an absence of initially spherical strain markers (Lisle, 1985).

The hyperbolic curve dictates how and where Rf/Ø curves plot on an Rf/Ø graph. Because Rs defines the position of the hyperbolic curve along the Rf axis and Ri determines the length of this curve, the shape of Rf/Ø curves is thus dictated by the value of Rs, and the curves' position along the Rf axis is controlled by Ri. Once the value of Rs is determined for each sample face, the value of Ri can be varied. As Ri is successively increased, Rf/Ø curves plot progressively higher along the Rf axis, thus enclosing more data points. The Ri value that produces an Rf/Ø curve that best fits (i.e. encloses greater than 60% of the data points) is taken to be the mean Ri for that face.

Different geometric shapes of the curves provide information on varying degrees of strain imposed (Rs) and preferred orientation of strain markers. Figure 15 graphically depicts the variation of curve geometry and general interpretations can be made. Points that show a large fluctuation of Ø , for example, and do not cluster about a maximum Rf are fitted with the straight-dashed curve, indicating that the sample has unmeasurable strain and no preferred orientation. Points the show a small fluctuation of Ø and cluster about a maximum Rf are fitted with the dash-square curve, indicating the sample has high strain and preferred orientation that is well pronounced.

To some extent the choice of Rf/Ø curves, and thus the choice of Rs and Ri, are subjective and rely on visual best fit (Lisle, 1985). Because a range of Rs and Ri values can generate an identical

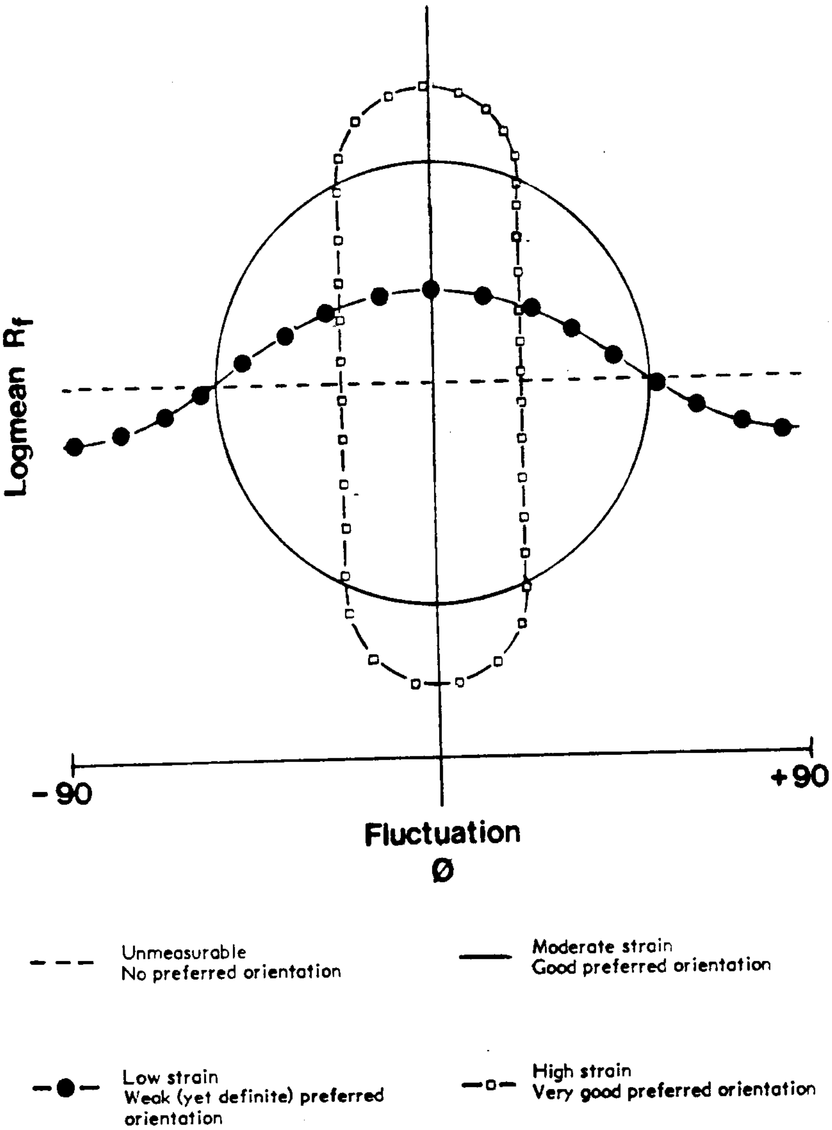

Figure 15. Rf/Φ example graph explaining significance of different Rf/Φ curve geometries.

distribution of symmetry, an independent internal check is necessary to enable measurement of these values. Lisle (1977) recommended the use of Theta curves when applying Dunnet's (1969) Rf/Ø technique as a more objective procedure for fitting theoretical curves to find Rs and Ri. Application of Theta curves also provides an internal check against misapplication of the Rf/Ø proceedure (Lisle, 1977). An ammendment to the Rf/Ø program, the Theta curve method has been developed and computerized to compensate for previous shortcomings (Lisle, 1977; Peach and Lisle, 1979; Borradaile, 1984).

The THETA program objectively determines Rs by successively destraining the elliptical markers. The increment of destraining that gives the most random distribution of marker orientations is R(s). The unstraining process consists of the superposition of a reciprocal strain ellipse on each deformed strain marker (Rf/Ø), the pre-strain marker then being a product of the superposition (Peach et al., 1979). The direction perpendicular to the principal extention direction (i.e. vector mean of the long axes of the strained particles) is used as the unstraining direction (Borradaile,1984). To destrain each chondrule, the reciprocal strain is altered in magnitude in increments of 0.05 from (H = +0.6) to (H = -2.0), where H is the harmonic mean of the deformed marker Rf values (Peach et al., 1979). At each stage of destraining, the chondrules are statistically analyzed for the presence of a still present preferred orientation (Peach et al., 1979). The strain that imposes the most isotropic distribution of strain marker orientations is taken to be the reciprocal strain ellipse for that face. After destraining, a statistical test is applied to check the hypothesis that the mean Theta value (predeformational orientation) calculated for each face represents a sample from a population with random orientation. The chi-square (X2) test involves grouping Theta values for each chondrule into classes of similarity defined by a progression of theta curves. A graph of chi-square versus the destraining ratio (Rs) is generated allowing the goodness of fit of the theta curves to the data to be quantified. A vertical line on this graph denotes the 5% significance level of chi-square. Beyond this line, the lowest chi-square value corresponding with the strain ratio (Rs) of the reciprocal strain is taken to be the axial ratio of the provisional strain ellipse. A minimum chi-square value greater than the 5% significance level indicates a probable predeformational fabric. Once each sample face has been successively destrained, the axial ratios of chondrules in their "destrained state", are measured. The arithmetic mean of these ratios is taken to be the mean Ri for each face.

Three-dimensional analysis of finite homogeneous strain from deformed objects has generally required two-dimensional sections to be cut in principal planes of the finite strain ellipsoid (Ramsey, 1967; Dunnet, 1969; Dunnet and Siddans, 1971). Siddans (1980) developed a mathematical model that enables determination of a finite strain ellipsoids' axial magnitudes and principal orientation directions from three randomly oriented orthogonal faces on non-principal planes. The PASE 5 program based on Siddans (1980) utilizes ratio and orientation of the apparent strain ellipse on three perpendicular sections to calculate the best fit mean ellipsoid for the sample. The two-dimensional, perpendicular strain ellipse data used in the PASE 5 program is acquired from both the Rf/∅ and Ri/θ files. Through a series of three by three matrix transformations, this program generates a best fit finite strain ellipsoid and a best fit pre-strain ellipsoid. The axial ratios and orientations of these two ellipsoids should be the same if they succeed in providing independent internal checks for one another. The PASE 5 program initially requests specification of strike and dip of the planar section (ab) (Fig. 16). Because the initial orientation of ordinary chondrites is unknown, values of 0° strike and 0° dip were used as defined by the arbitrary reference frame previously established. The operator then provides Rf and ∅ or Ri and θ from the ellipse data for the ab, bc, and ca planes. The program provides six independent three-dimensional combinations of the two-dimensional strain data. These possible solutions are used to compute the best fit finite mean strain and pre-strain ellipsoids axial magnitudes and orientations. The shape of the ellipsoids are qualitatively depicted on a Flinn diagram whose abscissa is defined as the ratio of the intermediate to minimum axes B/C and ordinate as the ratio of the maximum to intermediate axes A/B. The K line identifies plane strain and divides the diagram into two fields of strain. An ellipsoid in the field above the K line has its B axis shortened, thus it is described as a prolate spheroid. An ellipsoid plotting in the field below the K line has its B axis extended, thus it is described as an oblate spheroid. The program also plots axial orientations of the possible solutions on an equal area stereonet.

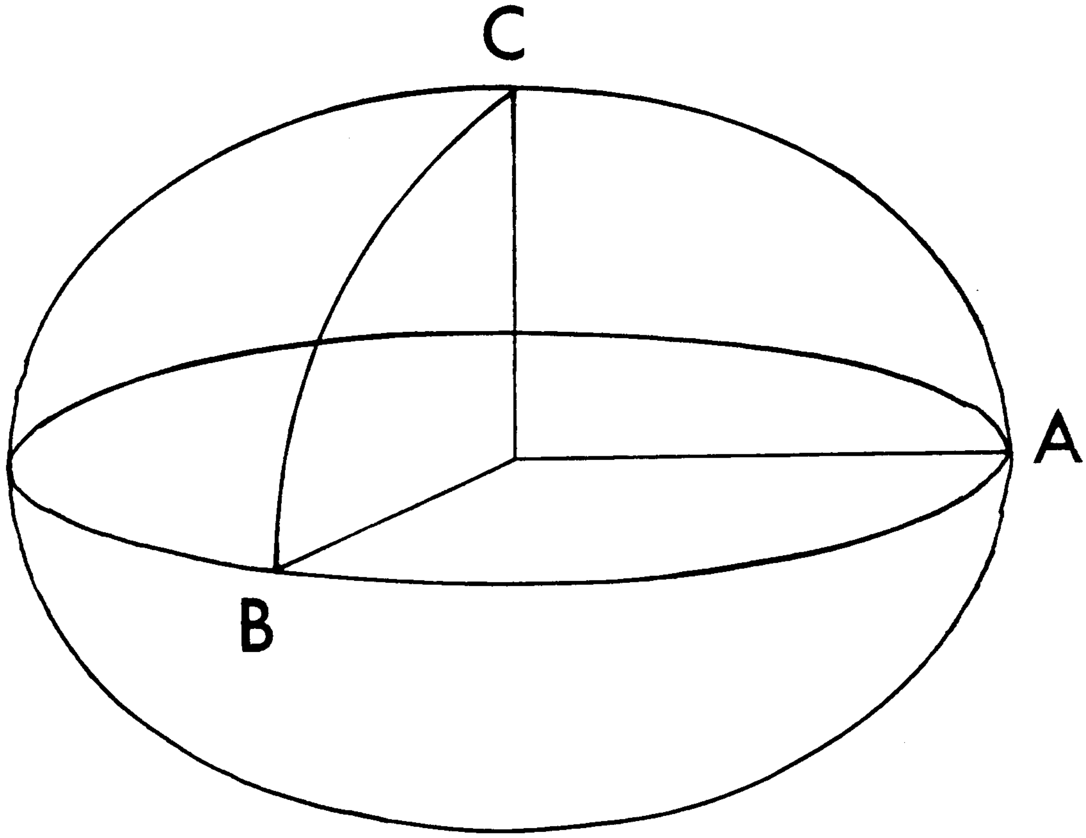

Figure 16. An oblate ellipsoids principle radii.

c = minimum

b = intermediate

a = maximum

Rf/Ø Data

Rf and Ø data for Mezo-Madaras, McKinney, Adrian, and Kelly. Sample faces are presented in the order: ab, bc and ca.

ab

MEZO-MADARAS (H)

AXIAL RATIO	LONG AXIS ORIENT.	AXIAL RATIO	LONG AXIS ORIENT.
1.27	-81.30	1.66	-81.24
1.39	-80.89	1.02	-76.31
1.13	-75.39	1.37	-73.53
1.42	-73.07	1.43	-57.58
1.53	-54.86	1.36	-51.25
1.27	-47.66	1.73	-42.36
1.47	-40.31	1.62	-39.19
1.11	-25.97	1.13	-24.83
1.08	-22.93	1.55	-21.81
1.07	-21.64	1.15	-15.23
1.54	-15.11	1.17	-14.26
1.13	-11.79	1.21	-10.94
1.06	-7.55	1.17	-6.22
1.18	-6.16	1.22	-1.58
1.36	+11.97	1.96	+18.08
1.62	+20.04	1.36	+20.28
1.38	+21.38	1.32	+23.75
1.13	+25.92	1.27	+26.17
1.30	+32.99	1.15	+33.90
1.53	+37.59	1.27	+42.98
1.74	+57.56	1.37	+57.76
1.26	+59.91	1.52	+62.17
1.39	+65.86	1.23	+70.75
1.62	+71.81	1.39	+73.47
1.17	+73.91	1.11	+83.02

bc

MEZO-MADARAS (H)

AXIAL RATIO	LONG AXIS ORIENT.	AXIAL RATIO	LONG AXIS ORIENT.
1.15	-82.47	1.67	-76.56
1.81	-69.28	1.29	-62.74
1.02	-59.92	1.51	-46.85
1.32	-39.55	1.45	-33.07
1.64	-27.51	1.52	-24.35
1.22	-23.54	1.42	-21.22
1.59	-20.84	1.47	-19.44
1.43	-17.55	1.52	-16.79
1.95	-16.17	1.60	-15.61
1.41	-13.75	1.37	-13.45
1.67	-12.60	1.17	-12.08
1.53	-11.94	1.50	-10.39
2.49	-8.81	1.37	-8.74
1.26	-5.44	1.16	-4.86
1.34	-2.93	1.60	-2.24
1.25	-0.58	1.32	+0.04
1.58	+1.80	1.56	+1.99
1.73	+2.19	1.05	+2.29
1.62	+2.74	1.83	+2.76
1.39	+5.85	2.00	+7.36
1.15	+7.83	1.23	+10.61
1.22	+11.16	1.35	+23.89
1.68	+32.10	1.40	+40.61
1.16	+75.42	1.04	+77.38
1.14	+78.62	1.34	+81.10

MEZO-MADARAS (H)

ca

AXIAL RATIO	LONG AXIS ORIENT.	AXIAL RATIO	LONG AXIS ORIENT.
1.32	-40.24	1.49	-39.89
1.03	-21.87	1.20	+0.78
1.92	+4.34	1.70	+25.30
1.32	+27.90	1.91	+28.93
1.46	+28.97	1.77	+29.48
1.73	+30.88	1.79	+32.96
1.82	+34.15	1.61	+36.02
1.28	+39.90	1.44	+40.78
1.59	+40.92	1.27	+42.31
1.72	+43.08	1.23	+43.41
1.61	+43.73	1.65	+43.75
1.55	+44.86	1.33	+45.31
1.49	+47.28	1.22	+47.28
1.98	+47.78	1.42	+47.78
1.58	+48.46	1.37	+48.53
1.24	+49.01	1.74	+49.98
1.33	+50.22	1.46	+50.75
1.56	+50.97	1.71	+53.20
1.19	+53.90	1.39	+54.77
1.24	+55.56	1.25	+57.09
1.44	+57.14	1.62	+57.32
1.43	+57.94	1.15	+60.97
1.19	+63.10	1.60	+65.11
1.90	+65.74	1.51	+69.10
2.59	+70.17	1.14	+70.34
1.11	+72.86	1.78	+74.51
1.98	+78.44	1.18	+83.84
1.10	+86.00	1.47	+87.85
1.53	-72.99	1.05	-53.90
1.17	-51.54		

ab McKINNEY

AXIAL RATIO	LONG AXIS ORIENT.	AXIAL RATIO	LONG AXIS ORIENT.
1.03	+44.73	1.15	+45.69
1.81	+50.77	1.11	+65.26
1.52	+66.70	1.28	+80.08
1.67	+81.63	2.23	+82.57
1.68	+85.20	1.49	+85.82
1.30	+87.17	1.43	-85.23
1.64	-84.48	1.46	-79.00
1.42	-77.33	1.61	-76.97
2.01	-75.19	1.29	-74.60
1.52	-73.30	1.25	-73.17
1.50	-72.91	1.33	-72.02
3.03	-71.43	1.50	-71.11
1.96	-68.50	1.84	-68.32
1.38	-67.49	1.84	-65.99
1.34	-65.13	1.24	-64.44
1.88	-63.30	1.09	-63.04
1.76	-61.57	2.61	-61.36
1.20	-60.48	1.93	-60.00
2.54	-59.85	1.81	-58.77
1.49	-58.75	1.46	-57.96
1.07	-57.39	2.61	-54.99
1.72	-54.23	1.63	-53.84
1.92	-52.66	1.38	-51.81
1.61	-50.28	1.38	-48.09
1.34	-47.98	1.88	-45.95
1.29	-43.85	1.41	-42.75
1.62	-40.72	1.50	-40.48
1.74	-24.39	1.07	-22.93
1.26	-19.17	1.22	-13.49
1.39	-4.14	1.19	+21.83

bc

McKINNEY

AXIAL RATIO	LONG AXIS ORIENT.	AXIAL RATIO	LONG AXIS ORIENT.
1.43	+41.33	1.46	+43.35
1.76	+55.20	1.27	+56.00
1.23	+57.13	1.54	+60.81
1.81	+60.88	1.34	+69.20
1.26	+71.42	1.28	+75.00
1.64	+75.36	1.36	+76.00
1.49	+77.46	1.29	+80.60
1.46	+81.28	1.17	+89.76
1.07	+89.79	1.22	-89.81
1.45	-87.50	1.73	-85.63
1.38	-85.21	1.19	-85.03
1.34	-82.78	1.21	-82.77
1.06	-78.80	1.28	-77.78
1.22	-75.03	2.35	-73.00
1.30	-72.33	1.74	-71.44
1.19	-69.61	1.13	-69.30
1.44	-68.58	1.17	-67.69
1.52	-65.07	1.56	-65.06
1.90	-62.12	1.76	-59.57
1.45	-59.02	1.37	-57.63
1.34	-57.42	1.15	-53.75
1.38	-51.74	1.67	-51.27
1.36	-50.34	1.20	-47.27
1.41	-43.90	1.47	-43.58
2.32	-43.14	1.30	-41.06
1.19	-37.92	3.10	-36.23
3.34	-35.92	1.44	-35.80
1.90	-34.33	1.20	-33.72
1.71	-33.04	1.18	-32.24
1.13	-32.14	1.07	-31.58
1.68	-30.62	1.55	-30.27

bc

1.52	-29.43	1.40	-29.16
1.56	-28.30	1.55	-17.57
1.51	-16.65	1.42	-9.43
1.78	-8.49	1.41	-7.73
1.07	-6.86	1.11	-2.57
2.02	+1.78	1.95	+2.10
1.87	+4.20	1.26	+8.64
1.83	+14.34	1.35	+15.06
1.96	+27.00	1.17	+29.66

AXIAL RATIO	LONG AXIS ORIENT.	AXIAL RATIO	LONG AXIS ORIENT.
1.49	-96.95	1.19	-86.33
1.13	-85.56	1.37	-78.93
1.15	-78.55	1.22	-76.34
1.19	-67.25	1.60	-65.74
1.62	-51.09	1.64	-50.36
1.10	-46.48	1.12	-39.99
1.49	-39.78	1.67	-36.73
1.38	-36.17	2.04	-31.84
1.04	-31.00	1.19	-25.23
1.34	-24.82	1.15	-24.28
1.19	-20.60	1.27	-18.50
1.58	-16.00	1.55	-11.79
2.14	-11.79	1.17	-8.44
1.49	-7.90	1.02	-7.77
1.27	-6.40	1.77	-3.71
1.23	-3.47	1.11	-1.75
1.37	+1.62	1.26	+2.17
1.53	+2.52	1.35	+4.69
1.33	+7.66	1.57	+11.36
1.65	+12.83	1.41	+16.08
1.19	+17.32	1.45	+18.12
1.25	+21.51	1.61	+23.48
2.22	+26.40	1.59	+32.74
1.24	+35.42	1.04	+40.22
1.06	+52.43	1.15	+54.16
1.22	+54.88	1.58	+55.27
1.08	+59.57	1.07	+60.41
1.26	+62.72	1.15	+68.65
1.17	+77.00	1.43	+81.98
1.35	+85.49	1.40	+86.27

ADRIAN

ab

AXIAL RATIO	LONG A[illegible]	[illegible]	[illegible]ONG AXI[illegible]
1.84	+87.43	[illegible]	+[illegible]8.07
1.52	+89.07	1.33	+88.42
1.26	-89.56	1.27	-87.83
1.21	-79.22	1.40	-74.87
1.12	-72.16	1.22	-63.31
1.11	-62.48	1.12	-59.99
1.17	-53.06	1.29	-51.36
1.24	-51.13	1.18	-50.05
1.05	-43.72	1.49	-39.92
2.21	-39.70	1.31	-37.24
1.04	-32.26	1.14	-30.80
1.05	-30.17	1.23	-27.72
1.38	-19.89	1.07	-18.77
1.26	-10.71	1.33	-10.03
1.40	-1.05	1.28	+3.49
1.43	+11.51	1.33	+12.13
1.16	+13.04	1.28	+13.58
1.11	+41.10	1.50	+48.64
1.30	+50.80	1.57	+53.06
1.11	+53.25	1.41	+54.85

bc

ADRIAN

AXIAL RATIO	[illegible]	[illegible]	[illegible]
1.09	[illegible]	[illegible]	+53.43
1.17	+67.52	[illegible]	+36.61
1.15	-97.76	1.43	-36.02
1.24	-82.47	1.22	-61.51
1.17	-60.90	1.36	-58.72
1.46	-55.19	1.51	-51.53
1.05	-50.65	1.85	-46.51
1.08	-45.90	1.17	-43.10
1.82	-41.44	1.35	-38.08
1.25	-39.06	1.15	-37.83
1.16	-36.88	1.04	-33.99
1.21	-30.94	1.32	-29.60
1.18	-25.96	1.55	-25.79
1.23	-14.54	1.37	-11.89
1.06	-9.79	1.97	-9.25
1.35	-6.08	1.17	-4.04
1.21	+2.85	1.20	+12.36
1.37	+13.05	1.24	+34.82
1.21	+37.27	1.23	+39.44
1.08	+40.74	1.14	+53.05

88

ca

ADRIAN

AXIAL RATIO	LONG AXIS ORIENT.	AXIAL RATIO	LONG AXIS ORIENT.
1.07	-89.95	1.09	-82.61
1.11	-81.72	1.13	-79.21
1.04	-70.70	1.19	-68.67
1.13	-69.49	1.13	-67.89
1.16	-56.93	1.29	-55.93
1.23	-51.01	1.11	-46.00
1.18	-39.34	1.06	-36.93
1.64	-30.38	1.45	-29.15
1.40	-29.02	1.13	-22.19
1.27	-13.67	1.45	-12.64
1.19	-8.98	1.20	-4.43
1.22	-3.01	1.13	+12.52
1.10	+17.57	1.25	+23.43
1.12	+25.28	1.07	+26.54
1.30	+34.38	1.11	+51.68

AXIAL RATIO	LONG AXIS ORIENT.	AXIAL RATIO	LONG AXIS ORIENT.
1.12	+84.75	1.08	+86.61
1.11	+89.33	1.20	-89.05
1.06	-80.04	1.10	-62.69
1.10	-61.38	1.33	-59.36
1.26	-58.27	1.30	-55.28
1.13	-53.31	1.16	-51.28
1.20	-49.79	1.43	-36.95
1.24	-28.09	1.24	-23.40
1.12	-18.78	1.21	-16.75
1.14	-11.03	1.16	-10.20
1.11	-8.71	1.44	-0.57
1.12	+20.85	1.18	+25.00
1.19	+36.08		

KELLY

bc

AXIAL RATIO	LONG AXIS ORIENT.	AXIAL RATIO	LONG AXIS ORIENT.
1.09	-81.97	1.30	-70.44
1.51	-61.00	1.13	-59.63
1.19	-51.57	1.10	-35.02
1.05	-31.72	1.13	-24.69
1.15	-20.31	1.10	-18.31
1.17	-12.58	1.21	-7.93
1.14	-4.80	1.04	+1.70
1.04	+21.86	1.43	+22.52
1.08	+51.03	1.07	+53.01
1.11	+64.58	1.07	+73.61

ca

KELLY

AXIAL RATIO	LONG AXIS ORIENT.	AXIAL RATIO	LONG AXIS ORIENT.
1.04	+85.60	1.23	-83.71
1.13	-58.65	1.46	-51.91
1.16	-41.67	1.12	-40.99
1.43	-38.30	1.22	-30.88
1.46	-18.57	1.35	-18.02
1.19	-11.46	1.18	-7.05
1.37	+0.66	1.38	+2.44
1.04	+6.04	1.11	+37.26
1.15	+37.63	1.28	+39.29
1.32	+59.54	1.43	+65.93

APPENDIX II

MEZO-MADARAS (S)

MMUHE
68 DATA POINTS
FLUCTUATION = 175
LOGMEAN Rf = 1.400
ORIGINAL ZERO = -6.704

TRY AN Rs ESTIMATE.....
Rs Ri = 1.28,1.35

SYMMETRY.....

12 16

18 13
Hard copy now
Press <RETURN> when ready

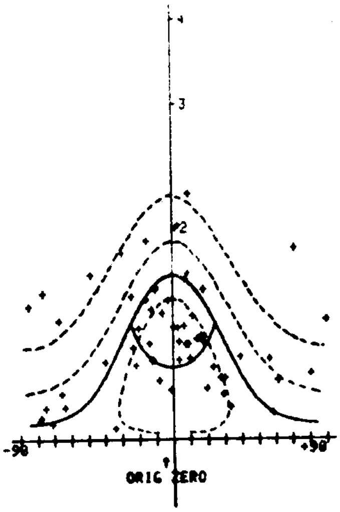

MMER?
68 DATA POINTS
FLUCTUATION = 176
LOGMEAN Rf = 1.7?2
ORIGINAL ZERO = 41.15?

TRY AN Rs ESTIMATE.....
Rs Ri = 1.27,1.3

SYMMETRY.....

14 11

16 18

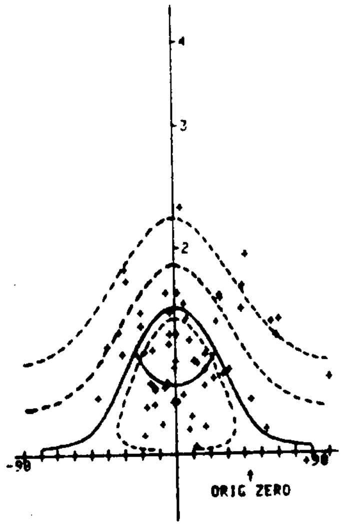

MMMAC
58 DATA POINTS
FLUCTUATION = 175
LOGMEAN Rf = 1.317
ORIGINAL ZERO = 55.066

TRY AN Rs ESTIMATE.....
Rs Ri = 1.15,1.3

SYMMETRY.....

18 11

11 17
Hard copy now
Press <RETURN> when ready

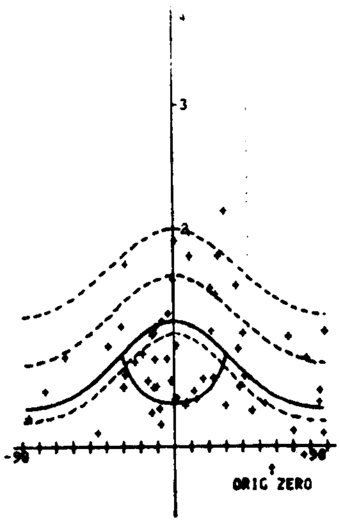

BARRATTA

bdab[illegible]
9[illegible] DATA [illegible]
FLUCTUATI[illegible] 14[illegible]
LOGMEAN R[illegible] = 1.4[illegible]
ORIGINAL ZERO = [illegible].45[illegible]

TRY AN Rs ESTIMATE.....
Rs Ri = 1.2[illegible].45

SYMMETRY.....

26 17

19 27

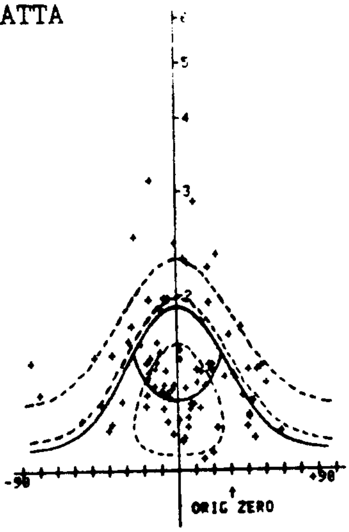

BNBC[illegible]
5[illegible] DATA POINT[illegible]
FLUCTUATI[illegible] 1[illegible]
LOGMEAN R[illegible] = 1.[illegible]
ORIGINAL ZERO = [illegible]0.4[illegible]

TRY AN Rs ESTIMATE.....
Rs Ri = 1.227,1.3

SYMMETRY.....

18 11

11 18

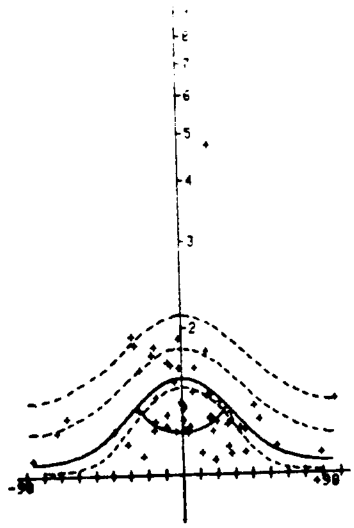

BECA[illegible]
[illegible] DATA [illegible]
FLUCTUATION = 1[illegible]4
LOGMEAN R[illegible] = 1.[illegible]14
ORIGINAL ZERO = [illegible].2[illegible]

TRY AN Rs ESTIMATE.....
Rs Ri = 1.09,1.35

SYMMETRY.....

26 17

17 29

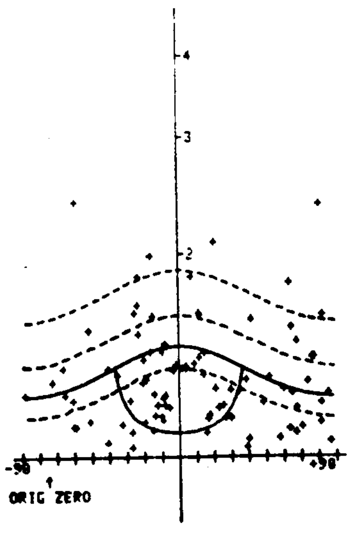

FARMINGTON

```
FARM UAB
35 DATA POINTS
FLUCTUATION = 126
LOGMEAN Rf =     1.410
ORIGINAL ZERO =   63.057


TRY AN Rs ESTIMATE.....
Rs Ri = 1.28,1.35


SYMMETRY.....

8  8

9  9
```

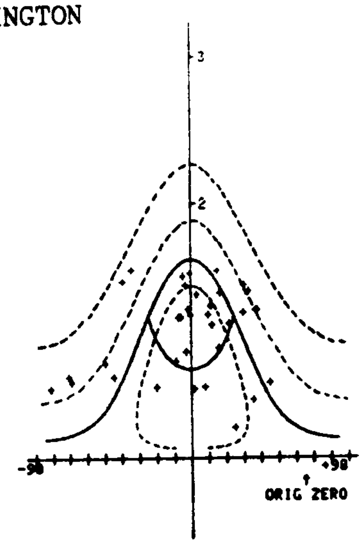


```
FARM EBC
40 DATA POINTS
FLUCTUATION = 164
LOGMEAN Rf =     1.419
ORIGINAL ZERO =   19.893


TRY AN Rs ESTIMATE.....
Rs Ri = 1.07,1.4


SYMMETRY.....

8   11

12   8
```

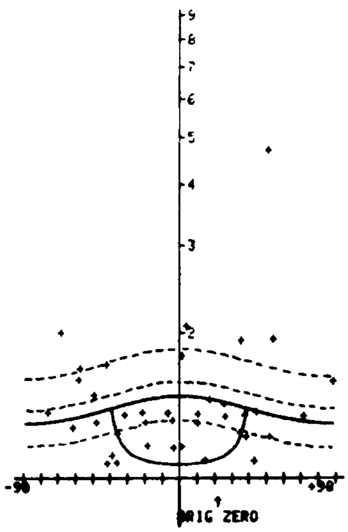


```
FARM NCA
20 DATA POINTS
FLUCTUATION = 145
LOGMEAN Rf =     1.434
ORIGINAL ZERO =  -19.221


TRY AN Rs ESTIMATE.....
Rs Ri = 1.15,1.45


SYMMETRY.....

5  4

5  5
```

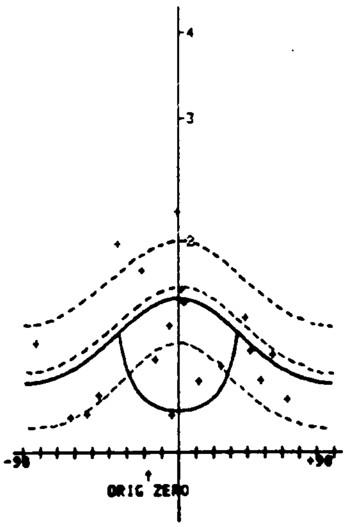

BROKEN BOW

BEEABDS
50 DATA POINTS
FLUCTUATION = 129
LOGMEAN Rf = 1.406
ORIGINAL ZERO = -25.323

TRY AN Rs ESTIMATE.....
Rs Ri = 1.21,1.35

SYMMETRY.....

11 13

14 11

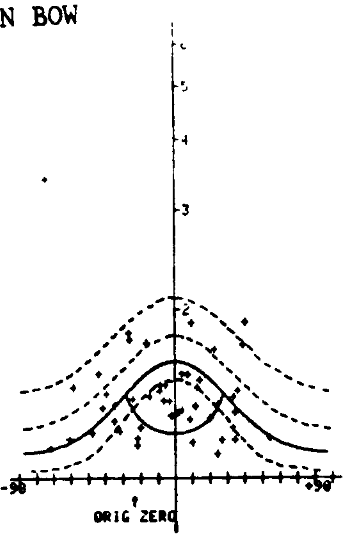

BBUBC
[illegible]
[illegible]
LOGMEAN Rf = [illegible]
ORIGINAL ZERO = [illegible]

TRY AN Rs ESTIMATE.....
Rs Ri = 1.24,1.3

SYMMETRY.....

16 9

9 15

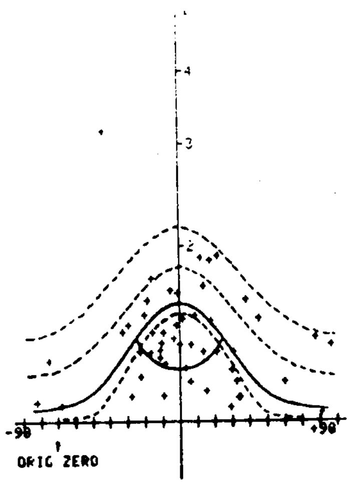

BE[illegible]
50 DATA POINTS
FLUCTUATION = 15[illegible]
LOGMEAN Rf = 1.34[illegible]
ORIGINAL ZERO = -24.[illegible]

TRY AN Rs ESTIMATE.....
Rs Ri = 1.07,1.35

SYMMETRY.....

12 14

13 10

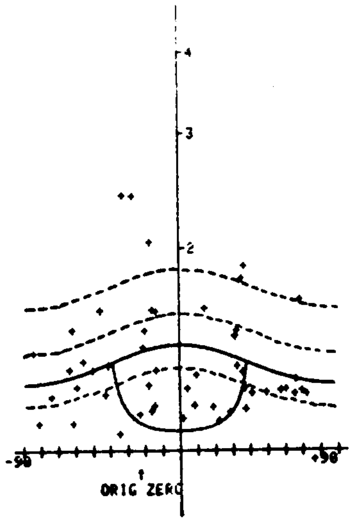

PARNALLEE

PARAB
90 DATA POINTS
FLUCTUATION = 165
LOGMEAN Rf = 1.363
ORIGINAL ZERO = -30.105

TRY AN Rs ESTIMATE.....
Rs Ri = 1.05,1.4

SYMMETRY.....

23 22

22 22

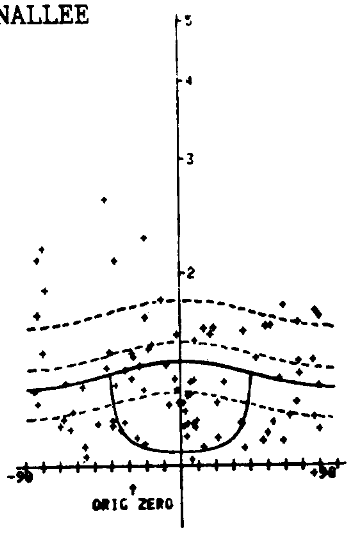

PARBC
90 DATA POINTS
FLUCTUATION = 167
LOGMEAN Rf = 1.472
ORIGINAL ZERO = -18.025

TRY AN Rs ESTIMATE.....
Rs Ri = 1.23,1.45

SYMMETRY.....

22 23

22 22

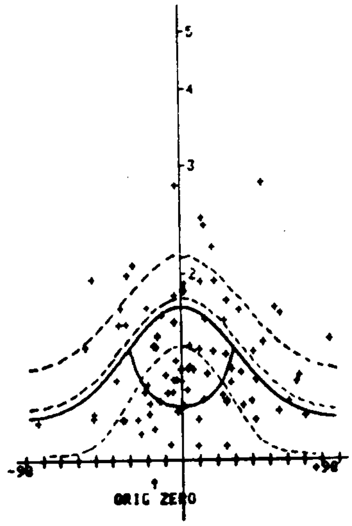

PARCA
85 DATA POINTS
FLUCTUATION = 172
LOGMEAN Rf = 1.352
ORIGINAL ZERO = 70.232

TRY AN Rs ESTIMATE.....
Rs Ri = 1.11,1.35

SYMMETRY.....

16 25

27 16

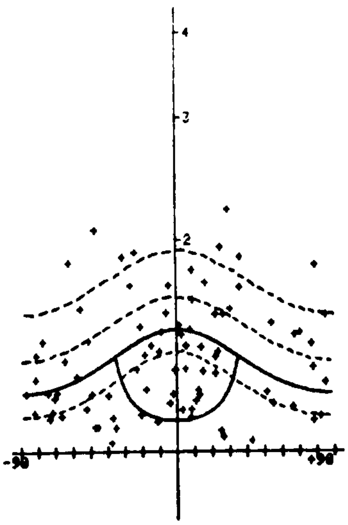

MENOW

```
Menow UHL
50 DATA POINTS
FLUCTUATION = 161
LOGMEAN Rf =    1.357
ORIGINAL ZERO =  -18.557


TRY AN Rs ESTIMATE.....
Rs Ri = 1.19,1.4


SYMMETRY.....

13   12

12   12
```

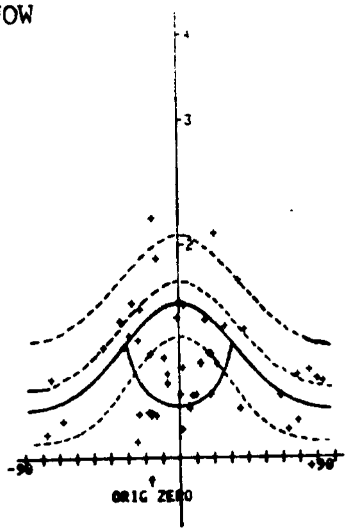


```
Menow EBC
40 DATA POINTS
FLUCTUATION = 170
LOGMEAN Rf =     1.259
ORIGINAL ZERO =    -4.934


TRY AN Rs ESTIMATE.....
Rs Ri = 1.03,1.3


SYMMETRY.....

9   11

11   8
```

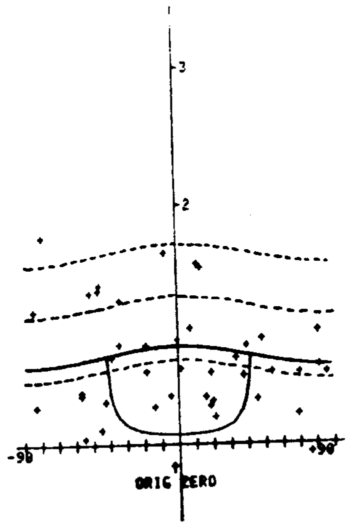


```
Menow HHC
50 DATA POINTS
FLUCTUATION = 160
LOGMEAN Rf =     1.2[illegible]
ORIGINAL ZERO =     -[illegible]39


TRY AN Rs ESTIMATE.....
Rs Ri = 1.13,1.25


SYMMETRY.....

11   13

14   11
Hard copy now
Press <RETURN> when ready
```

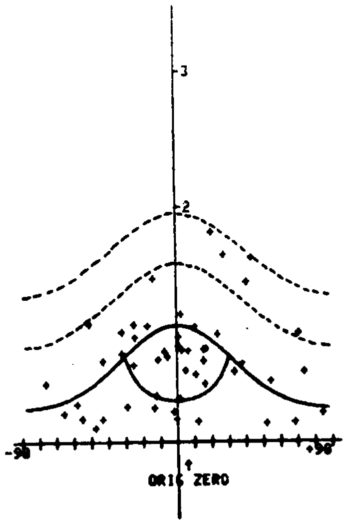

KESEN

KES EAB
45 [illegible]
FLUCTUATION = 16?
LOGMEAN Rf = 1.3??
ORIGINAL ZERO = 37.547

TRY AN Rs ESTIMATE.....
Rs Ri = 1.09,1.3

SYMMETRY.....

11 11

11 11

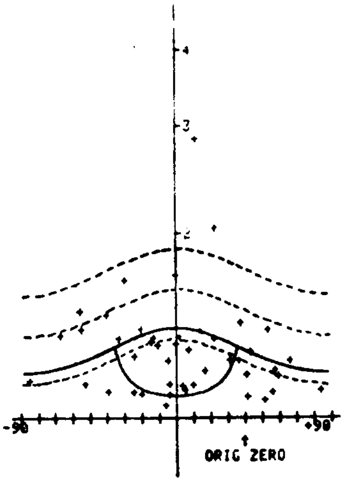

KES NBC
40 DATA POINTS
FLUCTUATION = 168
LOGMEAN Rf = 1.307
ORIGINAL ZERO = 32.293

TRY AN Rs ESTIMATE.....
Rs Ri = 1.12,1.3

SYMMETRY.....

11 9

9 11

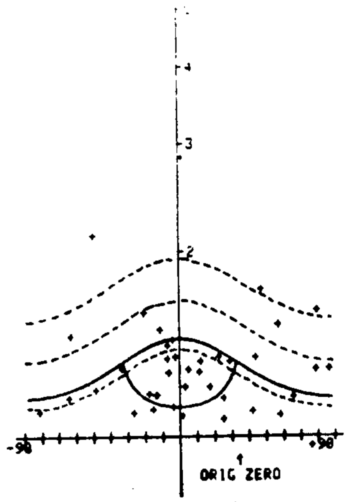

KES Uca
20 DATA POINTS
FLUCTUATION = 168
LOGMEAN Rf = 1.346
ORIGINAL ZERO = -2.646

TRY AN Rs ESTIMATE.....
Rs Ri = 1.03,1.45

SYMMETRY.....

5 5

6 4

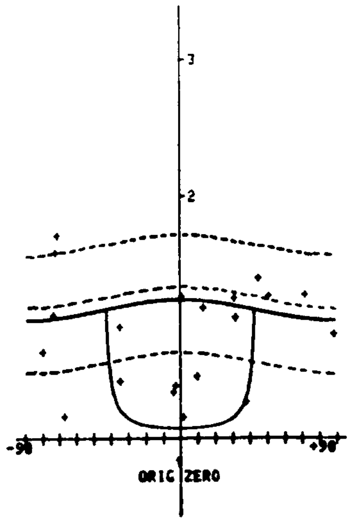

GRADY

GEABDS
65 DATA POINTS
FLUCTUATION = 172
LOGMEAN Rf = 1.226
ORIGINAL ZERO = 26.309

TRY AN Rs ESTIMATE.....
Rs Ri = 1.11,1.25

SYMMETRY.....

15 16

17 16
Hard copy now
Press <RETURN> when ready

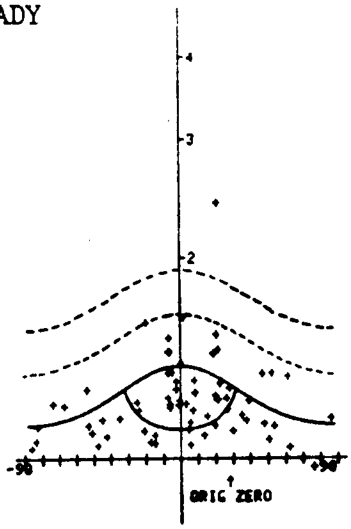

GNBCDS
5[illegible] DATA POINTS
FLUCTUATION = 15[illegible]
LOGMEAN Rf = 1.265
ORIGINAL ZERO = 73.100

TRY AN Rs ESTIMATE.....
Rs Ri = 1.14,1.4

SYMMETRY.....

14 15

15 14

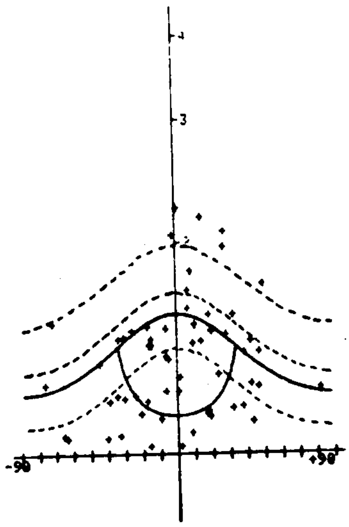

GUACDS
57 DATA POINTS
FLUCTUATION = 171
LOGMEAN Rf = 1.372
ORIGINAL ZERO = 57.346

TRY AN Rs ESTIMATE.....
Rs Ri = 1.07,1.45

SYMMETRY.....

13 14

15 14

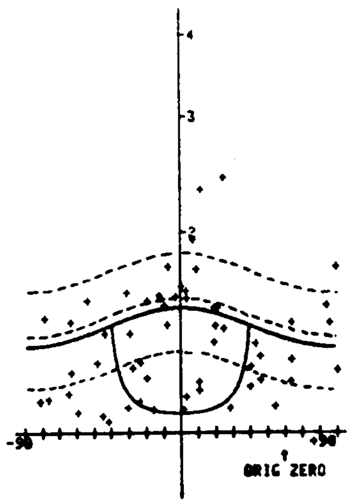

ANKOBER

ANK UAB
22 DATA POINTS
FLUCTUATION = 169
LOGMEAN Rf = 1.294
ORIGINAL ZERO = 31.516

TRY AN Rs ESTIMATE.....
Rs Ri = 1.89,1.35

SYMMETRY.....

6 4

5 6

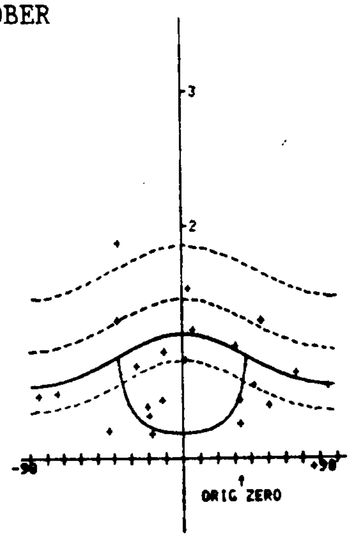

ANK NEC
45 DATA POINTS
FLUCTUATION = 162
LOGMEAN Rf = 1.316
ORIGINAL ZERO = 38.336

TRY AN Rs ESTIMATE.....
Rs Ri = 1.87,1.3

SYMMETRY.....

10 12

12 10

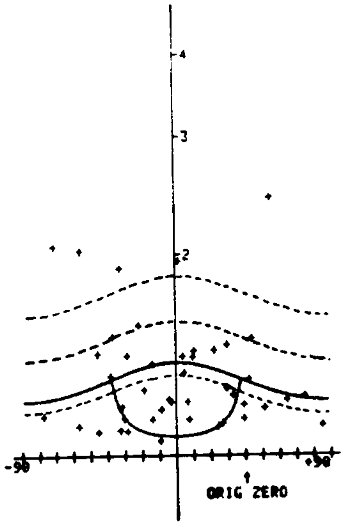

Ank EAC
42 DATA POINTS
FLUCTUATION = 175
LOGMEAN Rf = 1.379
ORIGINAL ZERO = 5.630

TRY AN Rs ESTIMATE.....
Rs Ri = 1.87,1.45

SYMMETRY.....

12 8

9 12

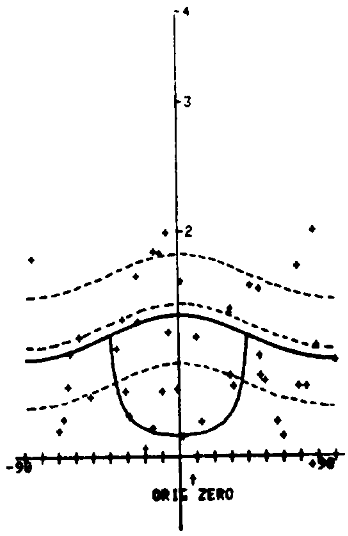

CLOVIS

```
CLOVIS UABB
60 DATA POINTS
FLUCTUATION = 154
LOGMEAN Rf =     1.266
ORIGINAL ZERO =    16.136

TRY AN Rs ESTIMATE.....
Rs Ri = 1.15,1.25

SYMMETRY.....

18   12

12   17
Hard copy now
Press <RETURN> when ready
```

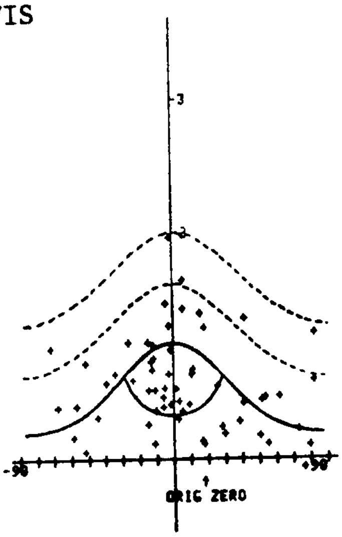


```
CLOVIS EBC
60 DATA POINTS
FLUCTUATION = 141
LOGMEAN Rf =     1.275
ORIGINAL ZERO =    13.662

TRY AN Rs ESTIMATE.....
Rs Ri =  1.14,1.25

SYMMETRY.....

12   10

18   11
```

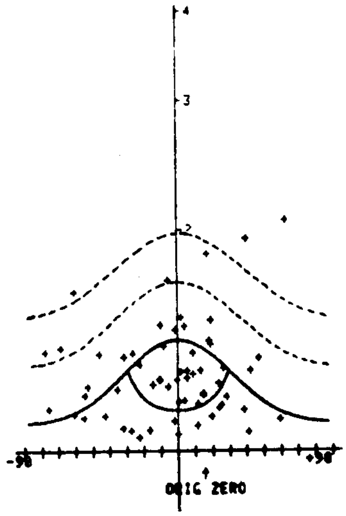


```
CLOVISNCA
64 DATA POINTS
FLUCTUATION = 170
LOGMEAN Rf =     1.296
ORIGINAL ZERO =    20.264

TRY AN Rs ESTIMATE.....
Rs Ri = 1.14,1.3

SYMMETRY.....

16   16

16   15
Hard copy now
Press <RETURN> when ready
```

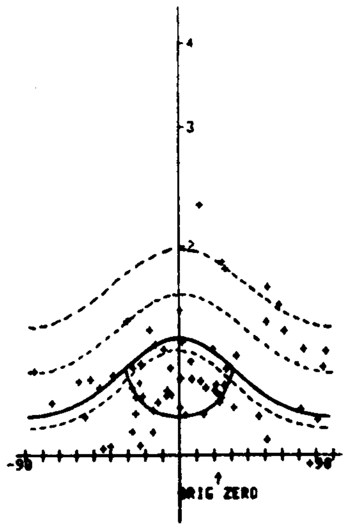

FAUCETT

FDABDS
65 DATA POINTS
FLUCTUATION = 155
LOGMEAN Rf = 1.269
ORIGINAL ZERO = 44.463

TRY AN Rs ESTIMATE.....
Rs Ri = 1.065,1.25

SYMMETRY.....

11 21

21 11
Hard copy now
Press <RETURN> when ready

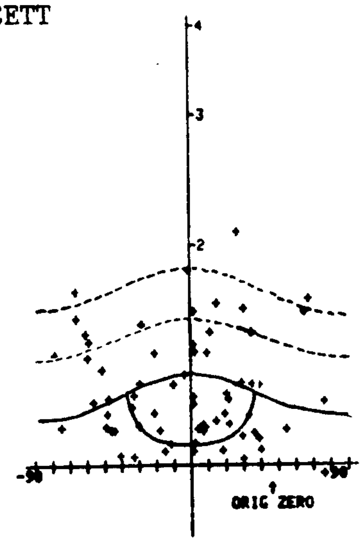

FNBCDS
51 DATA POINTS
FLUCTUATION = 177
LOGMEAN Rf = 1.297
ORIGINAL ZERO = 37.340

TRY AN Rs ESTIMATE.....
Rs Ri = 1.06,1.4

SYMMETRY.....

14 11

11 14
Hard copy now
Press <RETURN> when ready

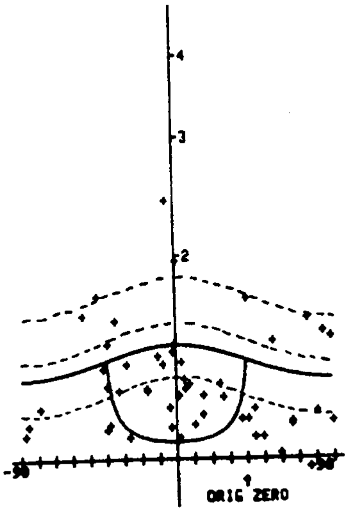

FECADS
70 DATA POINTS
FLUCTUATION = 156
LOGMEAN Rf = 1.309
ORIGINAL ZERO = 48.599

TRY AN Rs ESTIMATE.....
Rs Ri = 1.1,1.25

SYMMETRY.....

18 16

17 18
Hard copy now
Press <RETURN> when ready

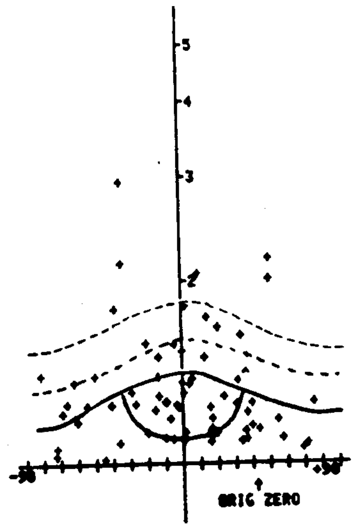

HAMMOND DOWNS

HDUAB
55 DATA POINTS
FLUCTUATION = 156
LOGMEAN Rf = 1.247
ORIGINAL ZERO = 12.384

TRY AN Rs ESTIMATE.....
Rs Ri = 1.07,1.25

SYMMETRY.....

16 10

11 17
Hard copy now
Press (RETURN) when ready

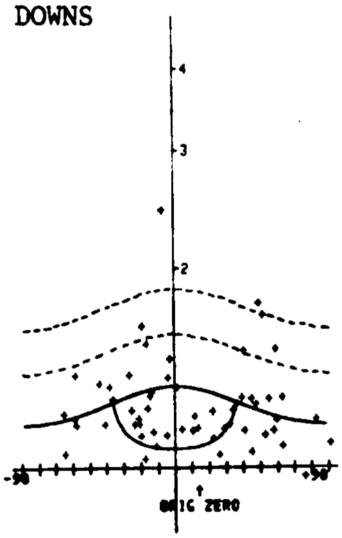

HDNBC
55 DATA POINTS
FLUCTUATION = 154
LOGMEAN Rf = 1.272
ORIGINAL ZERO = 9.237

TRY AN Rs ESTIMATE.....
Rs Ri = 1.13,1.3

SYMMETRY.....

13 13

14 14

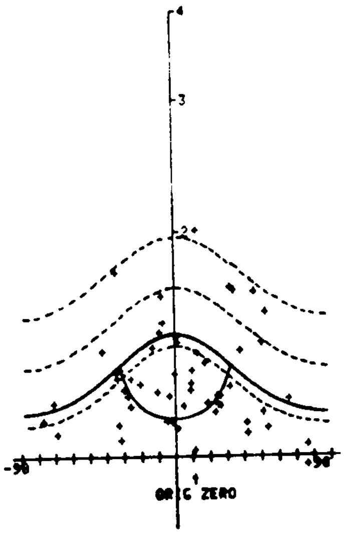

HDECA
55 DATA POINTS
FLUCTUATION = 169
LOGMEAN Rf = 1.239
ORIGINAL ZERO = 22.135

TRY AN Rs ESTIMATE.....
Rs Ri = 1.03,1.3

SYMMETRY.....

14 14

13 13

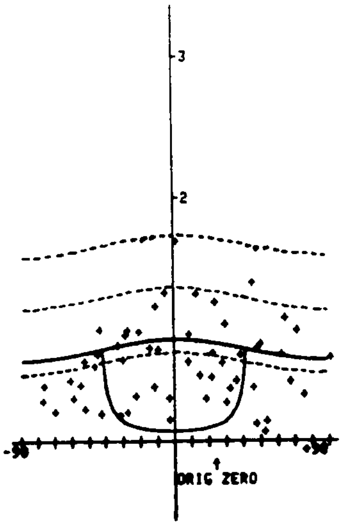

Table 7

Rs and Ri values from Rf/Phi and Theta data with their corresponding correlation coefficients

Meteorite	Rf/Phi Data: Rs,Ri			Theta Data: Rs,Ri			Corr. Coeff.	
	AB	BC	CA	AB	BC	CA	Rs	Ri
Mezo-Madaras (H)	1.05,1.45	1.30,1.30	1.39,1.35	1.05,1.36	1.25,1.34	1.24,1.34	0.95	0.95
Mezo-Madaras (S)	1.28,1.35	1.27,1.30	1.15,1.30	1.28,1.37	1.27,1.30	1.15,1.29	1.00	0.99
McKinney	1.34,1.40	1.13,1.50	1.11,1.35	1.30,1.40	1.12,1.46	1.07,1.35	0.99	0.99
Barratta	1.33,1.45	1.23,1.30	1.09,1.35	1.31,1.38		1.04,1.33		
Farmington	1.28,1.35	1.07,1.40	1.15,1.45	1.30,1.30	1.08,1.47	1.16,1.41	0.99	0.64
Broken Bow	1.21,1.35	1.24,1.30	1.07,1.35	1.18,1.36	1.16,1.34	1.02,1.37	0.96	0.95
Parnallee	1.05,1.40	1.23,1.45	1.11,1.35	1.09,1.40	1.24,1.40	1.03,1.34	0.82	0.87
Menow	1.19,1.40	1.03,1.30	1.03,1.25	1.19,1.30	1.03,1.29	1.15,1.24	0.70	0.85
Kesen	1.09,1.30	1.12,1.30	1.03,1.45	1.12,1.28	1.14,1.30	1.08,1.36	1.00	0.97
Grady	1.11,1.25	1.14,1.40	1.07,1.45	1.11,1.13	1.14,1.34	1.05,1.30	0.99	0.91
Ankober	1.08,1.35	1.07,1.30	1.07,1.45	1.08,1.29	1.09,1.32	1.06,1.40	0.99	0.83
Clovis	1.15,1.25	1.14,1.25	1.14,1.30	1.15,1.24	1.16,1.25	1.13,1.26	0.19	0.87
Faucett	1.07,1.25	1.06,1.40	1.10,1.25					
Hammond Downs	1.07,1.25	1.13,1.30	1.03,1.30	1.08,1.25	1.16,1.25	1.03,1.24	0.99	-.50
Adrian	1.05,1.30	1.08,1.25	1.05,1.25	1.02,1.29	1.11,1.27	1.04,1.19	0.98	0.65
Kelly	1.05,1.25	1.02,1.25	1.05,1.30	1.08,1.17	1.04,1.04	1.09,1.24	0.98	0.77

VITA

Deana Suzanne Sneyd was born in Peoria, Illinois on May 4, 1961. She attended elementary school, Junior High and was graduated from Warren Travis White Senior High School, in May 1979. The following September she entered the University of Texas, Austin, and in August 1984 she recieved a Bachelor of Science degree in Geology. In the fall of 1984 she was accepted at the University of Tennessee, Knoxville and began to study toward her Master's degree. This degree was awarded in March 1987.